NTNU – Trondheim
Norwegian University of
Science and Technology

Pulsed Laser Deposition of Zinc Sulfide Thin Films on Silicon

The influence of substrate orientation and preparation on thin film morphology and texture

Carl Philip J Heimdal

Physics
Submission date: May 2014
Supervisor: Turid Worren Reenaas, IFY

Norwegian University of Science and Technology
Department of Physics

Abstract

The effect of orientation and preparation of silicon substrates on the growth morphology and crystalline structure of ZnS thin films deposited by pulsed laser deposition (PLD) has been investigated through scanning electron microscopy (SEM) and grazing incidence x-ray diffraction (GIXRD). ZnS thin films were grown on silicon (100) and (111), on HF-treated and untreated silicon (100) as well as substrates coated with Al, Ge and Au. The ZnS films showed entirely different morphologies for ZnS films grown on silicon (100) and (111) substrates, but a preferred orientation largely independent of substrate orientation, preparation or coating. The films are either wurtzite (W) or a mixture of wurtzite or zinc blende (ZB). The preferred orientation is suggested to be related to the lower surface energies of the W(001) surface, and the ZB(111) surface in a Zn-poor environment.

A technique for in-situ removal of native oxide from silicon by laser ablation of a ZnS target was tested and found to remove a significant amount of the surface of the substrates.

The reoxidation in air of silicon (100) surfaces was monitored by ellipsometry, and HF-treated substrates were examined by RHEED. The results revealed that HF-treated Si(100) showed signs of rapid reoxidation in air, but this had no visible effect on ZnS film growth compared to untreated substrates.

Preface

This master's thesis was written during the fall of 2013 and the spring of 2014 as the conclusion of my masters degree in physics at the Norwegian University of Science and Technology, NTNU. The experimental work was performed at the Department of Physics, at the department of Materials Science and Engineering, as well as NTNU's Nanolab.

I would like to thank my supervisor Turid Worren Reenaas for her enthusiasm and for giving me and Peter Kusterle the opportunity to be included in a research group, even though we were "only" master's students. I would also like to thank Zahra Ghadyani for the ellipsometry experiments, the Nanolab staff for all the help with instruments, Mohammedreza Nematollahi and Xiaodong Yang for all the help they gave me and the things they taught me, Fredrik Martinsen, Stanislav Polyakov and Eric Karhu for the chats and interesting discussions, Peter Kusterle for all the fun times.

Abbreviations

Symbol	=	definition
DIW	=	De-Ionized Water
FWHM	=	Full Width at Half Maximum
HF	=	HydroFluoric
ITO	=	Indium Tin Oxide
MBE	=	Molecular Beam Epitaxy
PLD	=	Pulsed Laser Deposition
PVD	=	Physical Vapor Deposition
RFMS	=	Radio Frequency Magnetron Sputtering
RHEED	=	Reflection High Energy Electron Diffraction
SEM	=	Scanning Electron Microscope (Microscopy)
Si	=	Silicon
W	=	Wurtzite
ZB	=	Zinc Blende
ZnS	=	Zinc Sulfide

Table of Contents

Summary i

Preface iii

Abbreviations v

Table of Contents ix

1 Introduction 1

2 Theory and Background 3

2.1 Crystalline Solids 3
2.1.1 Silicon and zinc sulfide 5
2.1.2 Bond coordination and Si-ZnS interface 7
2.1.3 Lattice mismatch and thermal expansion 7
2.2 Thin film growth 8
2.2.1 Microstructure evolution and growth modes 9
2.3 Silicon substrate preparation 11
2.4 Pulsed Laser Deposition (PLD) 11
2.4.1 History 11
2.4.2 How does it work? 11
2.4.3 Target ablation and plasma plume 12
2.4.4 Plume kinetics 13
2.4.5 Deposition and nucleation 14
2.4.6 Laser and deposition parameters 14
2.5 Characterization 14
2.5.1 X-ray Diffraction (XRD) 14

2.5.2 Reflection High Energy Electron Diffraction (RHEED) 17
2.5.3 Profilometry 22
2.5.4 Scanning Electron Microscope (SEM) 22
2.5.5 Energy Dispersive X-ray Spectroscopy 22
2.5.6 Spectroscopic Ellipsometry (SE) 23

3 Experimental Details 27
3.1 Lab and cleanroom use 27
3.2 Pulsed Laser Deposition system 28
3.2.1 KrF Excimer Laser 29
3.2.2 Laser spot 29
3.2.3 Energy measurements 30
3.2.4 Substrate mounting and heater 31
3.2.5 Substrates 31
3.2.6 ZnS Target 31
3.2.7 General deposition procedure 32
3.3 Substrate preparation 32
3.4 Experiments 33
3.4.1 Substrate temperature 33
3.4.2 ZnS Target 33
3.4.3 ZnS thin film growth on silicon (100) and (111) substrates 33
3.4.4 Etched and unetched Si (100) susbtrates 34
3.4.5 In-situ oxide removal and ZnS film growth 34
3.4.6 ZnS thin film growth on coated Si(100) substrates 35
3.4.7 HF etching and ellipsometry measurements 36
3.4.8 Cleaned Si and RHEED imaging 37
3.5 Characterization 37
3.5.1 Film Thickness 37
3.5.2 X-ray diffraction and GIXRD 37
3.5.3 SEM 38
3.5.4 RHEED 38

4 Results 39
4.1 Penetration depth of X-rays in ZnS 39
4.2 ZnS target 40
4.3 ZnS thin films on Si (100) and (111) substrates 40
4.4 ZnS films on etched and unetched (100) silicon substrates 44
4.5 In-situ oxide removal and ZnS film growth 46
4.6 ZnS thin film growth on coated Si(100) substrates 48
4.7 Ellipsometry on etched Si(100) substrates 49

4.8 Cleaned Si and RHEED imaging 50

5 Discussion **51**
5.1 General Remarks 51
5.1.1 Diffraction peaks 51
5.2 ZnS Target 52
5.3 ZnS growth on silicon (100) and (111) 52
5.4 ZnS films on etched and unetched silicon (100) substrates 55
5.5 In-situ oxide removal and ZnS film growth 55
5.6 Thin film growth on coated silicon (100) substrates 56
5.7 Ellipsometry measurements on etched silicon substrates 56
5.8 Cleaned Si and RHEED imaging 57
5.9 Surface energies and preferred orientation 58
5.10 Size dependence of ZnS phase stability 58

6 Conclusion **59**
6.1 Epitaxial ZnS film growth 59
6.2 In-situ native oxide removal 59
6.3 Substrate preparation 59

7 Further Work **61**
7.1 General remarks 61
7.2 Experimental issues 61
7.2.1 Pressure gauge on the load lock 61
7.2.2 Heater, heater stage and transfer arm 62
7.2.3 Heater and sample mounting 62
7.2.4 RHEED equipment 62
7.3 Film thickness uniformity 63
7.4 Future ZnS growth on silicon and characterization 63
7.5 Substrate preparation 63

Bibliography **65**

Chapter 1

Introduction

In a semiconductor device such as a solar cell, it is desirable to produce a material in which generated charge carriers have a long lifetime. In order to have a long carrier lifetime, a low concentration of defects and impurities which create carrier recombination centres is needed. One good candidate for such a material, is a crystal. In a device such as a heterojunction solar cell, it is desirable to have crystalline layers of different materials on top of each other. This can be obtained by growing a crystalline layer on top of a crystalline substrate. However conceptually simple this may seem, it is not a trivial matter at all, and, in many cases, it is impossible to do without compromising the quality of the top crystal layer. High purity materials are needed, and their structural, thermal and electronic properties must be similar to some degree. Much research has been devoted to growing high quality crystal thin films on crystalline substrates, and a huge variety of deposition methods and combinations of materials and substrates exists.

Transparent conducting materials (TCMs) are important components of electronic devices such as thin films photovoltaics and light emitting diodes. Today, many of the materials used in thin film photovoltaics have the disatvantage of being scarce and expensive, such as ITO (Indium Tin Oxide), often used as a transparent conductive top layer in solar cells. In research on high efficiency solar cells, many other scarce and toxic compounds and/or heavy metals are also being researched, such as InAs/GaAs quantum dot structures [1], ZnTe intermediate band solar cells [2], or other technologies, such as CdS/CdTe thin film solar cells [3].

Zinc sulfide (ZnS): Zinc sulfide is a direct wide band gap semiconductor composed of earth-abundant elements and it is non-toxic. It is a promising candidate for replacing ITO as a p-type high conductivity transparent layer in solar cells [4]. It is also a candidate intermediate band material in a new type of high efficiency solar cells [5]. ZnS thin films

have been grown on many different substrates by Pulsed Laser Deposition (PLD) [4, 6–11]. However, since ZnS has two polytypes with cubic and hexagonal lattices, this raises the question of how to control the phase of a deposited film. Having an excellent lattice match with silicon in its cubic form makes silicon a good candidate as a substrate for epitaxial single crystal growth. Nevertheless, an explanation of the observed favoring of (111)-orientation of ZnS thin films (in the work done in our lab), even when grown on silicon (100), is not clear. ZnS thin films grown on amorphous quartz glass substrates have this same orientation [11, 12]. This makes one wonder if the problem might be the preparation of the substrate before deposition. If an amorphous oxide (which is much like glass) is still present on a silicon surface when film deposition starts, the influence of the substrate is obstructed.

Pulsed Laser Deposition (PLD): The beauty of Pulsed Laser Deposition as a thin film growth technique is its conceptual simplicity. Ever since the discovery of the first lasers in the 1960s, this technique has undergone tremendous development, and is now applicable for the deposition of a wide range of materials, from thin polymer films to superconductors, complex oxides, metals, biomaterials and many more [13]. Complete deposition systems can be bought, both for research purposes and large scale thin film manufacturing. PLD is a cheap and practically simple thin film deposition method, growing in popularity.

Scope of this project: This project has two main scopes. The first is to investigate several aspects of ZnS thin film growth on silicon by PLD, such as the influence on ZnS thin films of the substrate orientation and preparation. SEM imaging and X-ray diffraction will reveal crystal orientation and structure, as well as growth parameters and surface morphology. The second is to investigate preparation of silicon substrates and their reoxidation in air. Ex-situ ellipsometry will reveal the time evolution of the reoxidation of the surface, and in-situ RHEED images will give information on the surface structure of silicon substrates. An in-situ surface oxide removal technique will also be tested.

Chapter 2

Theory and Background

2.1 Crystalline Solids

A crystalline solid is a material whose constituents are arranged in an ordered pattern in three dimensions, such that each point of this three-dimensional lattice, has identical surroundings. There are only 14 ways to arrange points in such a way and these constitute the 14 Bravais lattices [14]. A general crystal lattice is described by the set of points given by the position vector $\mathbf{R}$;

$$\mathbf{R} = n_1\mathbf{a}_1 + n_2\mathbf{a}_2 + n_3\mathbf{a}_3, \tag{2.1}$$

where $n_{1,2,3}$ are integers and $\mathbf{a}_{1,2,3}$ are linearly independent primitive lattice vectors. A crystal is usually described by a lattice and a basis, where a basis gives additional atomic positions. The basis can be described by a set of vectors $\mathbf{u}_i$, so that any point in the crystal can be given as the sum of the Bravais position vector and a basis vector; $\mathbf{R} + \mathbf{u}_i$. Lattices can be broken into primitive cells, which is a distinct and repeated unit in the lattice described by the set of points

$$\mathbf{R} = x_1\mathbf{a}_1 + x_2\mathbf{a}_2 + x_3\mathbf{a}_3, \tag{2.2}$$

where $x_{1,2,3}$ are between 0 and 1. However, it is often hard to see symmetries using these cells, and a more common way to represent lattices by is by using conventional unit cells, as in figure 2.1 for the face-centerd cubic (fcc) and hexagonal lattices.

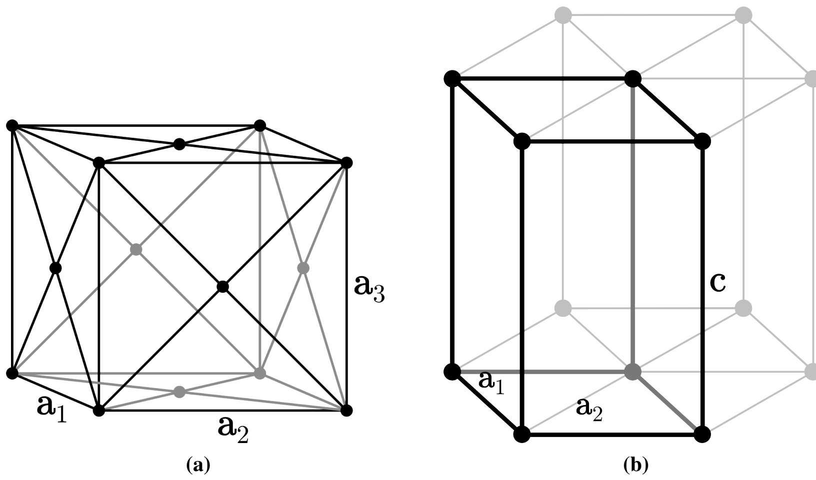

Figure 2.1: Conventional cells for (a) fcc and (b) hexagonal Bravais crystal lattices with lattice vectors [15, 16].

Diamond, zinc blende and wurtzite structures

The diamond structure is formed by adding a basis to the fcc structure (figure 2.1 (a)) with basis vectors

$$\mathbf{u}_1 = 0, \tag{2.3}$$

$$\mathbf{u}_2 = \frac{1}{4}\mathbf{a}_1 + \frac{1}{4}\mathbf{a}_2 + \frac{1}{4}\mathbf{a}_3. \tag{2.4}$$

If the two atoms are different, the structure is named zinc blende (ZB). Similarly, the wurtzite (W) structure is formed by adding a basis to the hexagonal lattice (figure 2.1 (b)) with basis vectors

$$\mathbf{u}_1 = 0\mathbf{a}_1 + 0\mathbf{a}_2 + 0\mathbf{c}, \tag{2.5}$$

$$\mathbf{u}_2 = \frac{1}{3}\mathbf{a}_1 + \frac{2}{3}\mathbf{a}_2 + \frac{1}{2}\mathbf{c}, \tag{2.6}$$

$$\mathbf{u}_3 = 0\mathbf{a}_1 + 0\mathbf{a}_2 + u\mathbf{c}, \tag{2.7}$$

$$\mathbf{u}_4 = \frac{1}{3}\mathbf{a}_1 + \frac{2}{3}\mathbf{a}_2 + \frac{1}{2} + u\mathbf{c}, \tag{2.8}$$

With $u \approx 3/8$ [17]. The first two positions in the basis are atoms of one element, and the other two atoms of a different element, such as zinc and sulfur in wurtzite ZnS.

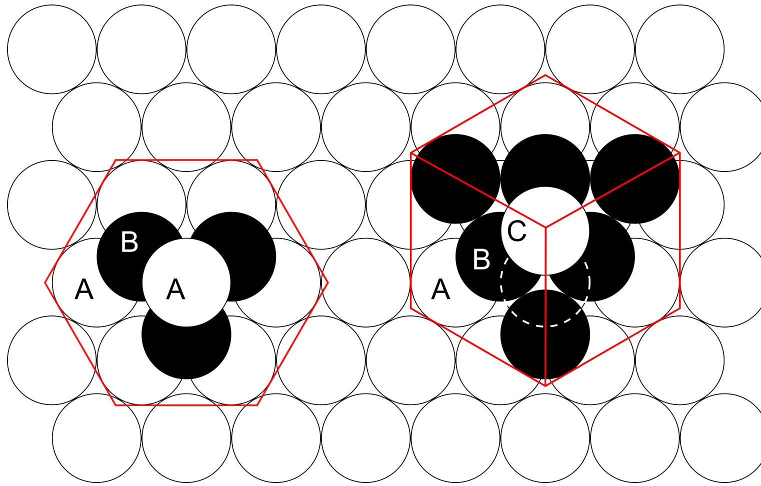

Figure 2.2: Fcc and hexagonal close-packing of spheres [18]. Hexagonal (left) and fcc (right) cells are enclosed by red lines, as seen from the [001] and [111] directions, rescpectively.

Close-packing of spheres

The fundamental difference between the zinc blende and wurtzite structures, is in the manner atoms are stacked on top of each other, illustrated in figure 2.2. The spheres (atoms) of the bottom layer are arranged at the vertices of triangular tiling. In the case of hexagonal packing, every other layer is identical, meaning a stacking sequence of ABABAB... In the case of fcc, the sequence of stacking planes follows a sequence ABCABC... If each sphere represents a dimer of Zn+S atoms, with the correct atomic positions this gives the wurtzite and zinc blende structures of zinc sulfide, respetively.

Miller Indices

Miller indices is an easy way to identify families of parallel crystal planes. They are defined by reducing the set

$$(hkl) = \left(\frac{a_1}{x_1} \frac{a_2}{x_2} \frac{a_3}{x_3} \right) \tag{2.9}$$

to lowest integers, where $x_{1,2,3}$ are the intercepts of the plane with the primitive vectors $\mathbf{a}_{1,2,3}$. In the special case of a cubic lattice, these indices give a vector normal to the plane in question. Directions in lattices are denoted [hkl] and planes by (hkl).

2.1.1 Silicon and zinc sulfide

Zinc sulfide is an inorganic, earth abundant, and non-toxic compound with the chemical formula ZnS. Zinc sulfide has two main crystalline forms, which have cubic and hexagonal

lattices. In the cubic form, ZnS has the zinc blende structure with a lattice constant of 5.420 Å and a band gap of 3.54 eV [19]. Its hexagonal form has a wurtzite structure with lattice constants $a = 3.82$ Å and $c = 6.26$ Å [19] and a band gap of 3.911 eV at 300 K [19]. The unit cells of these two structures are illustrated in figure 2.3 The transition from zinc blende to wurtzite structures normally occurs at about $1020\,°C$ [20].

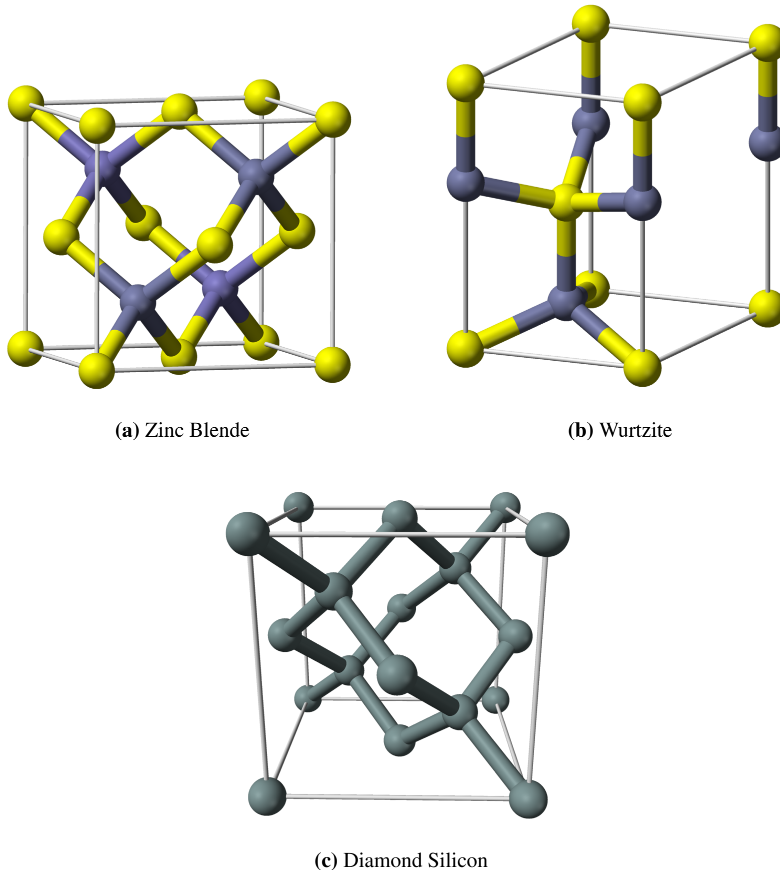

(a) Zinc Blende

(b) Wurtzite

(c) Diamond Silicon

Figure 2.3: Unit cells of (a) Zinc Blende, (b) Wurtzite and (c) Diamond Silicon. In (a) and (b), zinc atoms are grey and the sulfur atoms are yellow. The linked atoms bond in a tetrahedral coordination [21–23].

About 28.8 at.% of the earth's crust consists of silicon [24]. It is the second most abundant element in the crust (after oxygen), and it is non-toxic. It is mostly found in oxidized forms, such as SiO_2. Silicon in its pure crystal form has a diamond structure (figure 2.3), with a lattice constant of 5.431 Å at $22.5\,°C$ [25] and a band gap of 1.12 eV at 300 K [19].

2.1.2 Bond coordination and Si-ZnS interface

Silicon, and zinc sulfide in both its crystal forms, have a tetrahedral bond coordination as in figure 2.4.

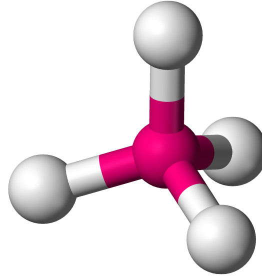

Figure 2.4: Illustration of a tetrahedral bond coordination. In silicon, each atom bonds to four other atoms. Simliarly, in zinc sulfide, each sulfur atom bonds to four zinc atoms, and each zinc atom bonds to four sulfur atoms. The surrounding atoms (grey) are all equidistant from the pink central atom, and the bond angles are about 109.5° [26].

In this configuration, silicon atoms, which have 4 valence electrons, share these in bonds with 4 surrounding atoms, meaning that there are 2 electrons per bond. For zinc sulfide, with zinc having 2 valence electrons and sulfur 6, also results in 2 electrons per bond. However, in counting valence electrons per bond for a Si-Zn bond results in 1.5 electrons per bond and for the Si-S bond it gives 2.5 electrons per bond. This tells that a tetrahedral bond configuration cannot be sustained across a Si/ZnS interface, and that a perfect interface between Si and ZnS is not to be expected, unless the electron configuration at the substrate in some way compensates for this, either by a specific orientation, or by introducing a compensating element [27].

2.1.3 Lattice mismatch and thermal expansion

It is easier to achieve high quality thin films with less crystal defects if the substrate and film have similar lattice constants. The relative lattice mismatch for ZB ZnS and silicon is

$$\frac{5.431 - 5.420}{5.431} \approx 0.002 = 0.2\%, \tag{2.10}$$

which is indeed a very low mismatch (a good match). However, the thermal expansion coefficients of silicon and zinc sulfide are quite different. This coefficient gives the relative deformation of the substance, as its temperature changes. For zinc sulfide it is $6.9 \cdot 10^{-6}\,\mathrm{K}^{-1}$ at $300\,\mathrm{K}$ [28] and for silicon it is $2.62 \cdot 10^{-6}\,\mathrm{K}$ at $300\,\mathrm{K}$ [19]. Because of this, the lattice mismatch will be different (higher) at temperatures other than $300\,\mathrm{K}$.

2.2 Thin film growth

A Physical Vapor Deposition (PVD) method, is a method for material deposition which involves evaporation and transfer of a solid or liquid source material onto a substrate where it solidifies. It is distinctly different from chemical vapor deposition (CVD) in that it is not a chemical reaction that produces the deposited material. Examples of PVD methods are molecular beam epitaxy (MBE), sputtering, evaporation electron beam PVD and PLD. The growth of a thin film by PVD can be described by a sequence of events in chronological order, starting from when an impinging particle (atom or molecule) reaches a surface [14, Chapter 5]. How particles behave and react with their environment, in each of these steps, affects the structural evolution of the thin film, and thus its final physical, optical and electronic properties.

Adatom and surface diffusion: When a particle reaches a surface, it interacts electronically with it. The impact reduces the particle's kinetic energy and adsorbtion onto the surface reduces its potential energy. On an ordered and clean surface such as that of a crystal, the adatom experiences a potential energy landscape which is highly periodic, caused by the arrangement of the surface atoms. If the surface is a semiconductor crystal, unsaturated bonds of the surface atoms will often have rearranged in a way that minimizes the surface energy. Such arrangements can give preferred directions for the diffusion of adatoms, since the surface energy becomes anisotropic. Adatoms may also reevaporate during film growth if they are highly energetic or if they are given extra energy by impinging particles.

Nucleation: The adatoms arriving on a flat surface will diffuse until they encounter other adatoms and form dimers, and eventually larger clusters. Their energy will be reduced, such that they become less mobile on the surface, and grow bigger, into clusters. When the probability of a new adatom attaching to an existing nucleus exceeds the probability of it forming a new nuclei, a critical nuclei density has been reached, and the next phase of film growth begins.

Island growth: The clusters formed on the surface in the initials stages of growth evolve in two ways; new adatoms coming directly from the adatom flux, and adatoms diffusing from the surface which is not yet fully covered. When different sized grains are close to each other, there will be an adatom concentration gradient on the surface between the grains, creating a driving force for diffusion giving rise to a net flux of adatoms towards the larger grain. This fenomenom is known as Ostwald ripening [14, Chapter 5.4]. Depending in part on what substrate is used, the very initial grains may have a random or preferred orientation. The orientations of these grains and the energetic properties of their surfaces can determine the preferred orientation seen in later stages of growth.

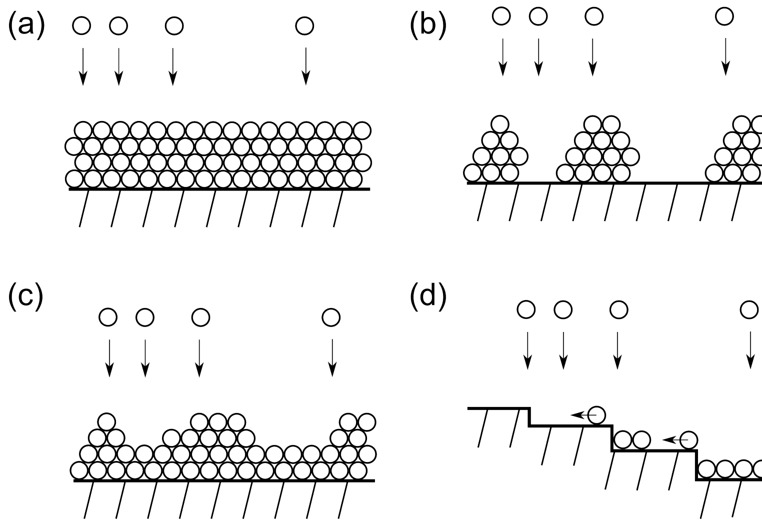

Figure 2.5: Thin film growth modes: (a) Frank-Van der Merwe (layer-by-layer), (b) Volmer-Weber (island growth), (c) Stranski-Krastanow (wetting layer + island growth), (d) Step-flow growth.

Coalescence: When islands grow larger than the distance between them, they will meet. When grains of different orientations, but similar sizes coalesce, the grain which has the lowest energy orientation will grow at the expense of the other. This increases the degree of preferred orientation in the film by further favoring low energy grain orientations. If these grains dominate the final thin film, their orientation will be the preferred orientation of the film.

2.2.1 Microstructure evolution and growth modes

When islands on the surface of a substrate have coalesced, the thin film entirely covers the susbtrate. Further growth of the film is decided by how new adatoms move on the facets of and between the already formed grains. Epitaxial growth is commonly described by the growth modes illustrated in figure 2.5.

The balance between the free energies of the film surface, γ_F, substrate surface, γ_S and interface between film and substrate, γ_I can be used to determine the growth mode [14, Chapter 5].

In the case of layer-by-layer growth (Fig. 2.5 (a)), $\gamma_F + \gamma_I < \gamma_S$. There is strong bonding between film and substrate, and/or diffusion is fast. Adatoms reaching the surface diffuse until they nucleate to form an entire layer.

If there is little or no bonding between the film and the substrate, the film cannot wet the substrate because this would lead to an increase in the total surface energy $\gamma_F + \gamma_I$. The bonding is stronger between species in the film than between film and substrate and/or

diffusion is slow. This results in three-dimensional island growth (Volmer-Weber, Fig. 2.5 (b)).

If the substrate and film are not lattice matched, an "intermediate" growth mode can occur in which there is an initial wetting layer, followed by island growth. This is Stranski-Krastanov growth (Fig. 2.5 (c)).

Figure 2.5 (d) shows step flow growth. Any susbtrate will not be perfectly flat, and there will be some steps on the surface. In this growth mode, adatoms diffuse to the step edges where they nucleate. This growth mode is more common at high temperatures and/or on vicinal substrates [29].

Structure Zones: As illustrated in figure 2.6, characterization of thin films reveal certains trends in microstructure, as a function of homologous temperature (the ratio of substrate temperature to the sublimation temperature, in this case of the thin film) and energy of impinging species [14, Chapter 5.6]. In figure 2.6 (a), the structures are divided into zones. With increasing temperature, the diffusivity also increases. In zone I, for low homologous temperatures, the structure is fibrous and columnar, with voids between columns. in zone II, there are large columnar grains with dense boundaries. In zone III, at temperatures close to the melting point, similar sized grains are formed, and they are no longer columnar, due to the recrystallization and segregation of impurities to grain boundaries. There is also an intermediate zone T, between zones I and II. Here, adatoms can diffuse enough to jump from grains of different orientations. Initially, grains are randomly oriented. But, since different surfaces have different diffusivities, there will be a net flux of adatoms from grains terminated by high mobility surfaces to grains terminated by low mobility surfaces. These latter grains will thus grow faster than the former. Eventually, the faster-growing grains will overgrow all others, giving rise to a strong preferred orientation of the final film.

Figure 2.6 (b) illustrates microstructure evolution as a funtion of the energy of the impinging species, for a constant temperature. The increase in kinetic energy of impinging particles leads to defect creation, which act as nucleation sites. With increased nucleation site density. the grain size naturally decreases.

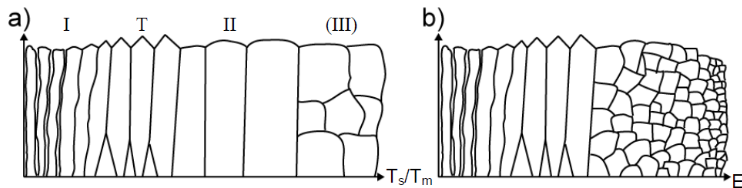

Figure 2.6: Structure zone diagrams. (a) shows the microstructural evolution as a function of homologous temperature (T_s/T_m). (b) shows the microstructural evolution as a function of the energy of the impinging species (E_i), at a single homologous temperature. Figure adopted from [30].

2.3 Silicon substrate preparation

Substrate preparation is a critical stage in preparing for deposition of crystalline semiconductors. Any silicon surface exposed to air or water which contains dissolved oxygen, will oxidize and a thin layer of amorphous silicon oxide ($SiO_x, x \leq 2$)[31, 32] will form on the surface. In moist air, molecular layers of moisture adsorb on the silicon surface within a second. Oxygen from the room is then dissolved into the adsorbed moisture layer and penetrates into the silicon, to form silicon dioxide. The thickness of this layer increases as the exposure time to air increases, but usually stabilizes at a thickness between 12 and 30 Å [33–39] because oxygen atoms at room temperature do not have sufficient energy to diffuse through this formed layer. A single monolayer of silicon oxide on a silicon wafer when starting a deposition, can lead to increased nucleation, defects and obstruction of epitaxial growth [40]. Undesired impurities and oxides on the surface can also result in poor device efficiency and bad adhesion between film and substrate. For silicon, there are a handful of common cleaning procedures, such as the RCA (Radio Corporation of America) clean, the modified Shiraki method, SPM and SPFM [41]. These involve wet chemical cleaning to remove organic and inorganic contaminants from the surface, and a final etch step to remove the native oxide before deposition.

2.4 Pulsed Laser Deposition (PLD)

2.4.1 History

The very first pulsed laser deposition experiments were carried out in the 1960s. But it was first during the 1980s that it was popularized by the work of Inam et. al [42], who deposited high temperature superconducting films with a complex stoichiometry with great success. The challenge when depositing multiple compound materials in other PVD techniques, is to have the correct stoichiometry while using elements with various evaporative properties. With PLD, this is adressed by simply enabling stoichiometric transfer from target to substrate. Today, PLD is a well known deposition technique, and entire ready-made systems can be bought from manufacturers specializing in PLD systems and equipment [43].

2.4.2 How does it work?

The basic principle of PLD is simple. Make a target with a desired composition, place it in a vacuum chamber together with a substrate onto which you want to deposit the target material. Fire a pulsed high energy density laser beam onto the target, and, voila! You have a thin film. Although the process of film deposition by PLD is somewhat more involved, this is the central idea.

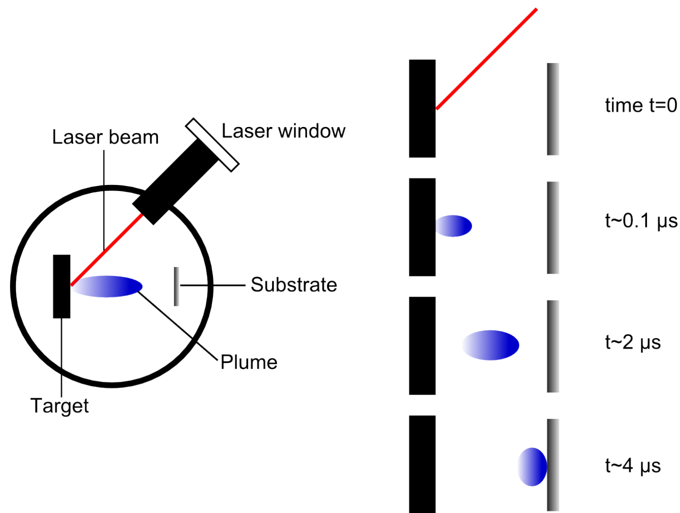

Figure 2.7: Schematic of the PLD process. At a time $t = 0$, a short $0.1 - 20$ ns high energy ($0.1 - 10$ J/cm^2) pulse hits the target. After about 1 μs, a plasma of atomic, diatomic, molecular and ionic species forms on the target surface. From about 2 to 4 μs, the plasma travels from the target and reaches the substrate surface. These numbers are only indicative, and may vary a lot between experiments. Figure adapted from [13].

A PLD process is illustated in figure 2.7. During deposition, a laser beam is directed through a focusing lens and then through a window into a vacuum chamber and onto a material target. PLD is a kinetically energetic physical deposition method, meaning that deposited species have a high kinetic energy. Depending on the composition and structure of the target, if the laser supplies enough energy, evaporation of target material occurs (ablation). This results in a plasma flow with high particle kinetic energy, centred around the direction perpendicular to the target surface, which is assumed flat. Usually, the substrate on which the target species are deposited, is parallel to the target, situated a few cm away from it. Deposition is either done in high vacuum or in the presence of an inert background gas, such as argon or helium, or other gases containing species desired in the deposited film, such as nitrogen or oxygen, either for doping [44] or structural variations such as oxygen in oxide films [45]. The powerful idea of PLD is that if you can make a target with a desired composition, you can make a thin film with the same composition, i.e., stoichiometric transfer between target and substrate.

2.4.3 Target ablation and plasma plume

For very low laser fluences, the laser would simpy heat the target, with ejected flux due to thermal evaporation. The vapor pressures of the target constituents would then decide the evaporative flux. When increasing the fluence there is a critical point called the ablation

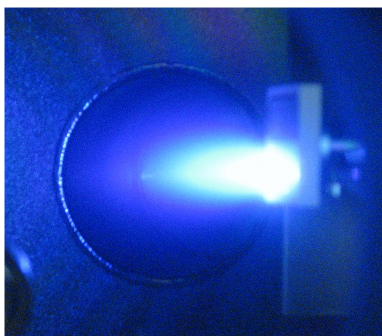

Figure 2.8: Picture of ZnS target during deposition.

threshold, where the energy absorbed from the laser is higher than the energy needed for evaporation. This threshold depends on the absorption coefficient of the material for the laser wavelength. The key to stoichiometric transfer between target and substrate in PLD, is choosing the laser wavelength and target material such that high energy densities are absorbed by the target, making the vaporization independent of the vapor pressures of the individual components of it.

Ablation of inorganic materials is typically done using a UV-laser with a nanosecond pulse duration, such as a KrF (Krypton Fluoride) 248 nm or XeCl (Xenon Chloride) 308 nm excimer laser. The vaporized volume on the target depends on the beam shape, size, and energy density, as well as the target density, composition and structure. The laser spot size is usually a few mm^2, and the penetration depth in the nanometer range. Under the right conditions, this process creates a plasma flow of atomic, diatomic and other low-mass species. Figure 2.8 shows a picture of the plume from a pressed an sintered ZnS powder target, hit by a 248 nm excimer laser.

2.4.4 Plume kinetics

The kinetic energies of the plume species in PLD are generally high, compared to other deposition techniques. They can be as low as 1eV, which is comparable to MBE, using a low laser fluence and/or a background gas, which slows the plume expansion. With higher laser energy, plume species energies up to several hundre eV's have been measured using time resolved spectroscopy during PLD [46]. The plume in PLD is highly directional, meaning that the distribution of material is not uniform around its center. This is an inherent disatvantage in PLD, resulting in a non-uniform film thickness. However, raster scanning of the laser beam across the target, using multiple spots, and/or scanning of the sample trough the plume can to some extent correct for this, enabling uniform deposition over large areas [47].

2.4.5 Deposition and nucleation

In PLD, as opposed to other in deposition techniques such as MBE and sputtering, the flow of particles onto the substrate is not continuous, but has a pulsed nature. However, theoretical and experimental studies indicate that PLD resembles MBE at low fluences [48, 49]. Also, in PLD, the growing film is not in thermodynamic equilibrium with the incoming species, so kinetic effects are important. The supersaturation resulting from the sudden bombardment of particles leads to a high nucleation density. Surface diffusion and surface and interface energies will then decide the growth mode.

2.4.6 Laser and deposition parameters

What makes PLD such a versatile technique, is the possibility of varying many parameters for a deposition.

Laser Parameters: The parameters which may vary with the choice of laser, beam path and optics are the laser wavelength, pulse energy, pulse frequency, pulse duration, beam shape and size and energy distribution in the beam. Pulse energy (fluence) and frequency, as well as beam shape and size are highly tunable parameters, whereas wavelength and pulse duration are inherent properties of the laser chosen.

Deposition Parameters: Given a target and substrate, the most important parameters for deposition are substrate temperature, distance from target to substrate, base pressure, and background pressure during deposition when a gas is introduced.

The optimization of the deposition of a selected material for a specific purpose, is a complex process which requires thorough experimentation by the systematic variation of deposition parameters, and a concise measure of film quality relevant to the purpose.

2.5 Characterization

2.5.1 X-ray Diffraction (XRD)

X-ray diffraction is a widely used and powerful non-destructive characterization technique which can potentially provide a lot of information about a sample without much specific sample preparation. The basic principle of XRD is the constructive and destructive interference of an ideal monochromatic and collimated X-ray beam in the atomic planes of the sample. The equation describing the occurrence of constructive interference is known as Braggs law [17];

$$n\lambda = 2d \sin\theta, \tag{2.11}$$

where n is an integer, λ is the X-ray wavelength, d is the spacing between atomic planes, and θ is the angle between the beam and the atomic planes, as illustrated in figure 2.9. Braggs law can be derived by geometric considerations, but is also a special case of the more general Laue condition from equation 2.20.

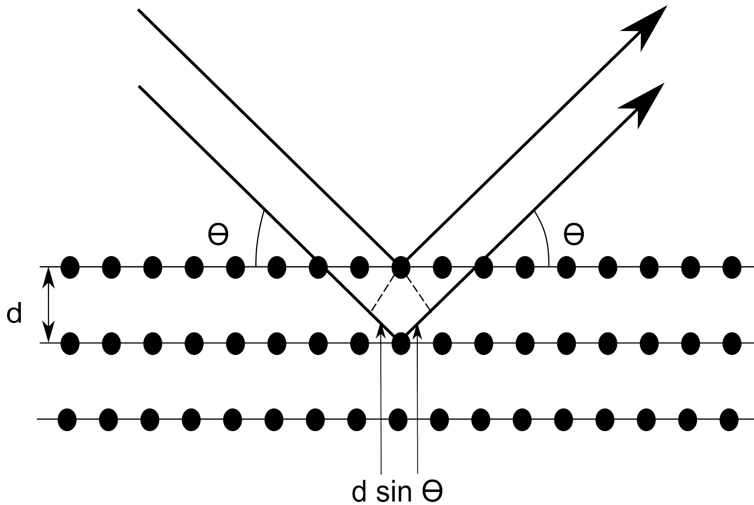

Figure 2.9: The geometry of Bragg's law. The condition for constructive interference is that the path length difference, $2d \sin \theta$, between the beams reflected from different atomic layers, is an integer multiple of the wavelength.

Grazing Incidence X-ray Diffraction

X-rays are not very surface sensitive. Their penetration depth is often of the order of micrometers, depending on the absorption of the material, and the wavelength used. Therefore, to characterise films thinner than their X-ray penetration depth, Grazing Incidence X-ray Diffraction (GIXRD) may be applied. In this technique, the X-ray beam is incident upon the sample at a very small angle α, usually no more than a few degrees, while a detector scans a 2θ range on the opposite side of the sample. The low and constant incidence angle gives a much lower vertical penetration depth of X-rays, and the diffraction volume is kept constant during the scan, making GIXRD suitable for probing thin films without getting a signal from the substrate. The theory of this section is taken from [17, p. 160-163].

Using the fact that the index of refraction of X-rays is slightly less than 1, it is possible to regulate the penetration depth by varying the angle of incidence. The penetration depth Λ_i is defined by

$$\frac{I}{I_0} = \frac{1}{e} = e^{-\mu \Lambda_i}, \tag{2.12}$$

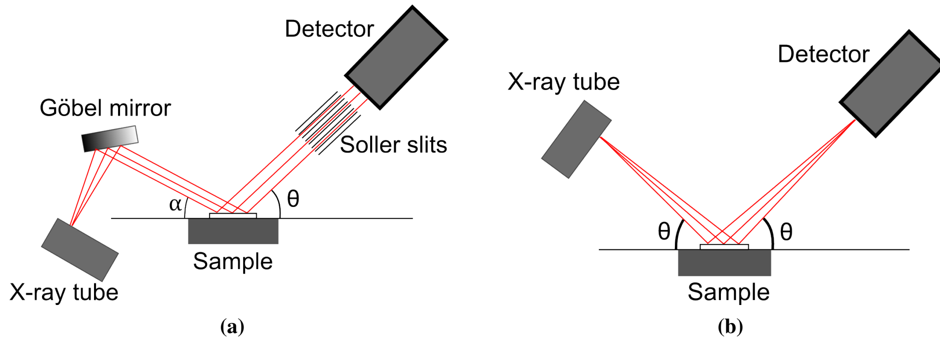

Figure 2.10: (a) Bragg-Brentano and (b) grazing incidence geometries.

where I and I_0 are the penetrating and incoming intensities, respectively. When the incidence angle is close to the critical angle, the penetration depth Λ_i can be shown to vary with the angle of incidence α_i as

$$\Lambda_i = \frac{\lambda}{2\pi\sqrt{2}}[((\alpha_i^2 - \alpha_c^2)^2 + 4\beta^2)^{1/2} + (\alpha_c^2 - \alpha_i^2)]^{-1/2}, \tag{2.13}$$

where $\beta = \lambda\mu/4\pi$, μ is the materials' linear absorption coefficient. α_c is the critical angle below which there is total reflection, and which is determined by Snell's law

$$\cos\alpha_c = 1 - |\delta|, \tag{2.14}$$

where δ is

$$\delta = -\rho r_0 \lambda^2/2\pi, \tag{2.15}$$

where ρ is the electron density, and r_0 is the classical electron radius (2.818 fm).

Bragg-Brentano and grazing incidence geometries

In investigations of polycrystalline samples, a $\theta/2\theta$ diffractometer is often used, where the angle of both the incoming and the exiting beam is θ with respect to the specimen surface, as in figure 2.10 (a). In GIXRD, the angle of the incoming beam is kept constant. It is common to use a Göbel mirror for collimating the beam before it hits the sample, because a normal divergent beam may diffract from the surroundings, such as the sample holder, and would also not be focused on the detector. A common practical approach to test whether there are spurious peaks in the diffraction pattern is to measure the uncoated substrate in the same configuration. Soller slits are also used before the detector to limit the out-of-plane divergence of the diffracted beam.

2.5.2 Reflection High Energy Electron Diffraction (RHEED)

Laue condition and Ewald construction

The reciprocal lattice to a set of primitive lattice vectors $\mathbf{a}_{1,2,3}$ is defined by

$$\mathbf{a}_j^* \cdot \mathbf{a}_i = 2\pi\delta_{ij}, \tag{2.16}$$

where δ_{ij} is the Kronecker delta and $\mathbf{a}_j^*$ and $\mathbf{a}_i$ are reciprocal and real lattice vectors, respectively. In reciprocal space, as in real space, we define lattice vectors by

$$\mathbf{G}_{hkl} = h\mathbf{a}_1^* + k\mathbf{a}_2^* + l\mathbf{a}_3^*, \tag{2.17}$$

And a scattering vector $\mathbf{Q}$ as

$$\mathbf{Q} = \mathbf{k}_f - \mathbf{k}_i, \tag{2.18}$$

that is, the difference between incoming and diffracted wave vectors. Since $|\mathbf{k}| = 2\pi/\lambda$, we have (see figure 2.11).

$$|\mathbf{Q}| = \frac{4\pi}{\lambda}\sin\theta \tag{2.19}$$

For constructive interference to occur, the phase difference between two waves has to be zero. It can be shown that the diffraction condition in reciprocal space, known as the Laue condition, is

$$\mathbf{Q} = \mathbf{G}. \tag{2.20}$$

In the kinematic approximation which considers elastic scattering, momentum and energy are conserved, meaning that

$$|\mathbf{k}_f| = |\mathbf{k}_i|, \tag{2.21}$$

$$\mathbf{k}_f - \mathbf{k}_i = \mathbf{G}. \tag{2.22}$$

Using this, we may construct a sphere of radius $|\mathbf{k}|$, centered at the start of $\mathbf{k}_i$ as shown for the two-dimensional case in figure 2.12.

Thus, constructive interference can only occur for reciprocal lattice points lying on the Ewald sphere (or circle).

RHEED

RHEED is a technique used to characterize the surface of crystalline materials. It is a grazing incidence technique which probes only the surface of a material, as opposed to

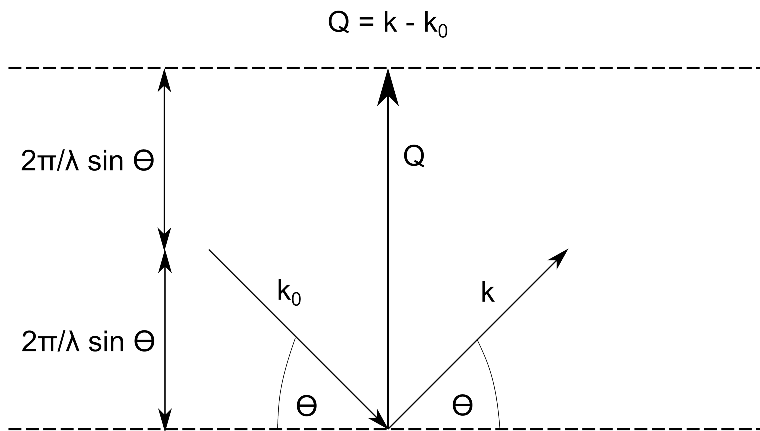

Figure 2.11: Geometry of scattering vector construction

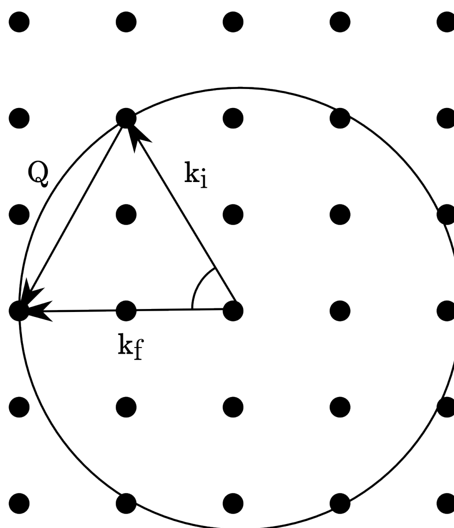

Figure 2.12: Two-dimensional Ewald construction. The diffraction condition is fulfilled when the scattering vector equals a reciprocal space vector.

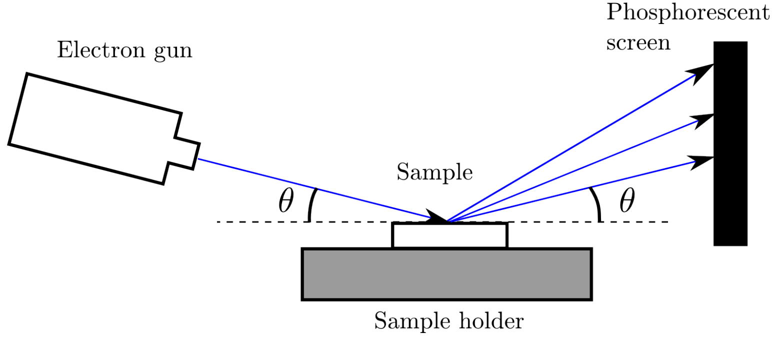

Figure 2.13: Schematic of a RHEED setup. The equipment is mounted onto a vacuum chamber.

other high energy electron characterisation techniques. Figure 2.13 shows a schematic of a RHEED setup. The theory of this section is taken from [50, Chapter 5].

In RHEED, only the very topmost layers contribute to scattering. Therefore we shall consider a two-dimensional lattice given by vectors

$$\mathbf{R}_n = n_1\mathbf{a}_1 + n_2\mathbf{a}_2, \tag{2.23}$$

where n_1 and n_2 are integers and $\mathbf{a}_1$ and $\mathbf{a}_2$ are the unit vectors of the surface primitive cell. Since there are only two real lattice vectors, the same applies for the reciprocal unit vectors.

$$\mathbf{a}_1^* = 2\pi\frac{\mathbf{a}_2 \times \hat{\mathbf{z}}}{\mathbf{a}_1 \cdot (\mathbf{a}_2 \times \hat{\mathbf{z}})} \tag{2.24}$$

$$\mathbf{a}_2^* = 2\pi\frac{\mathbf{a}_1 \times \hat{\mathbf{z}}}{\mathbf{a}_2 \cdot (\mathbf{a}_1 \times \hat{\mathbf{z}})} \tag{2.25}$$

A generalized reciprocal vector is then

$$\mathbf{B}_m = m_1\mathbf{a}_1^* + m_2\mathbf{a}_2^*, \tag{2.26}$$

where m_1 and m_2 are integers. The diffraction condition for a two-dimensional surface is illustrated in figure 2.14, by an adapted Ewald construction. In the two-dimensional case, since there is no diffraction condition in the direction perpendicular to the surface, the reciprocal lattice consists of infinitely long vertical rods separated by reciprocal lattice vectors. The intersection of these reciprocal lattice rods and the Ewald sphere, when projected onto the surface, give a reciprocal lattice vector $\mathbf{B}_m$, so the diffraction condition is fulfilled when

$$\mathbf{k}_{f,||} - \mathbf{k}_{i,||} = \mathbf{B}_m, \tag{2.27}$$

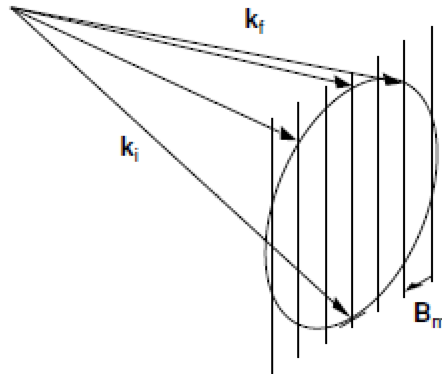

Figure 2.14: Ewald construction for RHEED. Both $\mathbf{k}_i$ and $\mathbf{k}_f$ extend from the center of the circle, which is a slice of the three-dimensional Ewald sphere of radius $|\mathbf{k}_i|$. Only the relevant reciprocal lattice rods are shown. Figure adopted from [50, Chapter 5].

where m is the mth diffracted beam. That is, when the difference in incident and final wave vectors, when projected onto the surface, equal a reciprocal lattice vector, analogous to the three-dimensional case. In the case of specular reflection, the incident and reflection angles are equal, and $\mathbf{B}_m = 0$, with the origin being defined by this. The corresponding reciprocal lattice vector is along the (00) rod. As seen from the viewpoint of the incident beam, the reflections to the right and left are labeled (01), (02)... and (0-1), (0-2), respectively (see figure 2.16 for an example from a silicon (100) surface).

Surface reconstruction

When a crystal is cut along a plane, the bonding at the surface differs from the bulk of the crystal in that there are dangling bonds, when the surface has not reacted with any other species from the surroundings. In order to minimize the surface energy, crystal surfaces tend to reconstruct, with surface atoms bonding together, lowering the number of dangling bonds. For silicon (100), two known surface reconstructions are illustrated in figure 2.15. (a) shows a silicon surface with two dangling bonds per atom, (b) shows the 2x1 reconstructed surface where the topmost atoms bond into dimers. The corresponding RHEED diffraction patterns are dinstinctly different in that going from a 1x1 reconstruction to a 2x1 reconstruction, viewed along the [110] azimuth, extra diffraction spots appear between the ones seen from a 1x1 reconstruction. This can be understood from the different in periodicity of the surface structure between the two. For the 2x1 reconstruction, the periodicity in the y-direction doubles compared to the 1x1 reconstruction, whereas the periodicity remains the same in the x-direction.

After cleaning and etching a silicon (100) substrate, heat treatment and monitoring

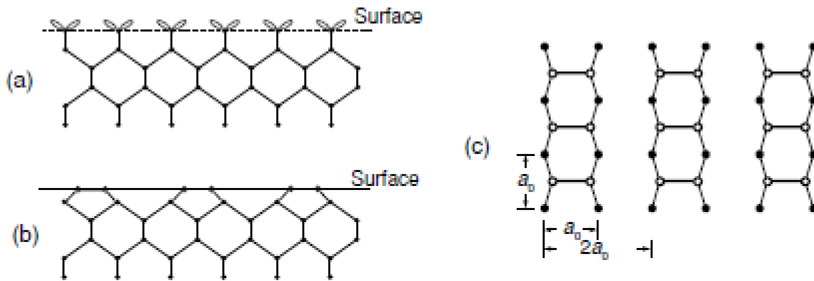

Figure 2.15: The surface reconstruction of a silicon (100) surface. (a): side view of 1x1 surface reconstruction; (b): side view of 2x1 surface reconstruction; (c): top view of 2x1 reconstruction. The white filled dots in the top views are the surface atoms which bond together in dimers. Figure adopted from [50, Chapter 5].

with RHEED is common. The observation of the 1x1 reconstruction followed by a 2x1 reconstruction after subsequent annealing is used as a "fingerprint" for a clean surface where hydrogen passivation has been desorbed. Instead of a calculation of the diffraction patterns of these surfaces, an image will be used as reference, shown in figure 2.16.

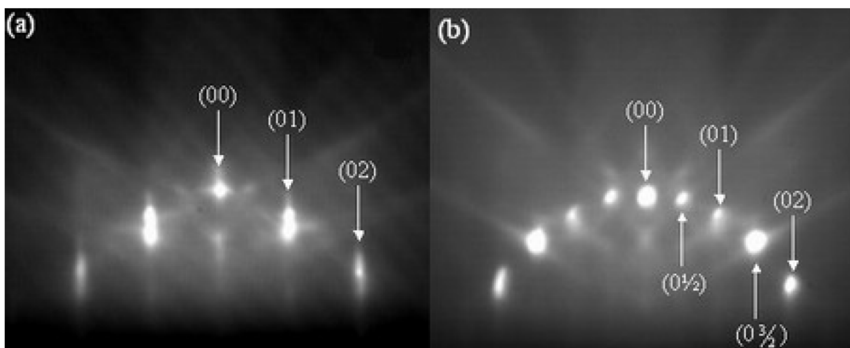

Figure 2.16: (a) Si (100)-1x1 obtained by chemically cleaning the sample and loading it to the vacuum within few minutes. (b) Si(100)-2x1 reconstructed surface obtained by chemically cleaning the sample and then baking the system for two days and flashing it up to 1200°C. Electron beam is incident in the <110>direction with 8.6 keV [51].

2.5.3 Profilometry

A profilometer allows for quick and easy profile and thickness measurements of e.g. deposited films on substrates. A contact stylus profilometer uses a sharp diamond tip with a small diameter that is moved vertically to make contact with the sample surface, and then it is scanned horizontally for a given range and tip force. The movement of the stylus across the sample surface, which is connected to a transducer, generates an electrical signal, which in turn can be converted to a digital signal that can be analysed on a computer.

2.5.4 Scanning Electron Microscope (SEM)

A scanning electron microscope is a microscope which sends high energy electrons (usually 1-30kV) in a focused beam onto a sample, and uses semiconductor detectors to image the sample. The resolution obtained, is in part determined by the energy (and thus wavelength) of the electrons. If the acceleration voltage of an SEM is set to 15 kV, the wavelength of an electron is then $\lambda = \frac{hc}{E} \approx 0.8$ Å. This does not however give a corresponding resolution of 0.8 Å. The resolution depends on the spot size and the interaction volume, which is the volume where electrons are ejected from. The best resolution is often obtained visualizing secondary electrons, which are ejected from the layer closest to the surface in the interaction volume, as seen in figure 2.17.

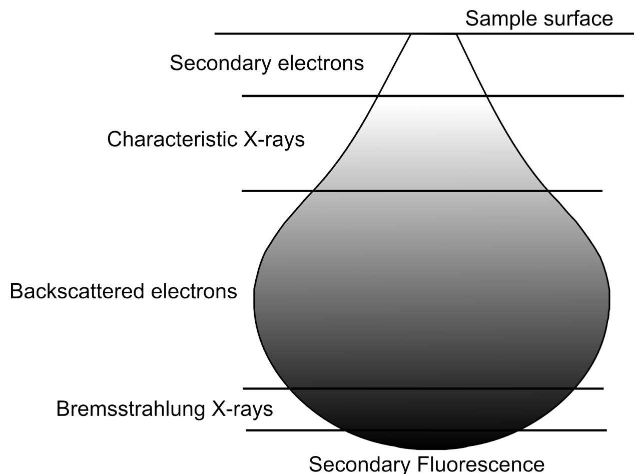

Figure 2.17: The interaction volume of high energy electrons as in an SEM.

2.5.5 Energy Dispersive X-ray Spectroscopy

Energy Dispersive X-ray Spectroscopy (EDS) is a characterization technique used for elemental analysis. It relies on the fact that each element has a unique atomic structure, and therefore also a unique set of peaks in its X-ray spectrum. To stimulate the emission of

these characteristic X-rays, a beam of high energy particles (such as electrons), or photons, is focused onto a specimen. Electrons in the specimen, which are initially in their ground states in discrete energy levels bound to the atoms (electron shells), may be excited by the incoming beam. This can result in an electron from an inner shell being excited, leaving behind an empty electron state, which in turn is filled by an electron from another higher energy shell. The filling of the empty state may result in emission of a characteristic X-ray photon, whose energy is equal to the difference in energy between the shells. Figure 2.17 indicates from which part of the electron interaction volume the emitted X-rays come from.

2.5.6 Spectroscopic Ellipsometry (SE)

This section gives an overview of spectroscopic ellipsometry, but does not cover details of the theory, relating measurements to models and physical parameters. The reason for this is that the complete theory is quite extensive, and that ellipsometry is not the main focus of this work. A more in-depth analysis can be found in [52].

Light polarization

Light consists of transverse oscillating electric and magnetic fields $\mathbf{E}$ and $\mathbf{B}$, which are orthogonal. Polarization of light is defined as the direction of the electric field. In a coordinate system where z is the direction of wave propagation, $\mathbf{E}$ can be written as a linear combination of x and y components:

$$\mathbf{E}(z,t) = E_x\hat{x} + E_y\hat{y}, \tag{2.28}$$

where

$$E_{x,y} = A_{x,y} = \cos(\omega t - kz + \phi_{x,y}). \tag{2.29}$$

$A_{x,y}$ are the amplitudes of the respective components, t is time, k is the wavenumber and $\phi_{x,y}$ are the phases of the components. What determines the polarization state is the relative phase and amplitude of these components. The most general case of polarization is elliptical polarization, illustrated in figure 2.18. The components of the electric field are out of phase and have different amplitudes, so that projection of $\mathbf{E}$ onto the xy-plane is an ellipse. A special case is when $A_x = A_y$, and $\phi = \pi/2 \pm n\pi$ for an integer n. This gives circularly polarized light, and $\mathbf{E}$ defines a circle when projected onto the xy-plane. If $\phi = \pi \pm n\pi$ for an integer n, and E_x and E_y have a linear dependence, the projection of $\mathbf{E}$ onto the xy-plane gives a straight line. This is linearly polarized light.

When light described by an electromagnetic wave with angular frequency ω hits a surface, it interacts with the free and bound electrons inside it. This process is governed by the complex dielectric functions $\epsilon(\omega)$ of the material. This function contains information on

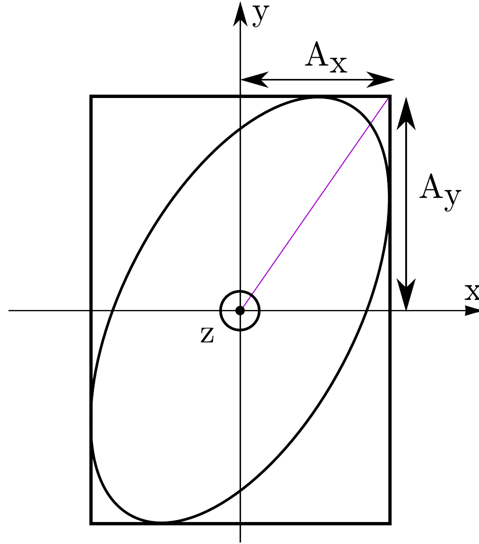

Figure 2.18: Illustration of elliptically polarized light. The z-axis is out of the paper. At any time $t = t_0$, the electric field amplitude is a vector starting at the z-axis, pointing to the ellipse. **E**, with respect to z and t, defines an ellipse when projected onto the xy-plane.

the optical properties of the material, as well as electrical and physical [52]. A schematic of an ellipsometry setup can be seen in figure 2.19. The light from the source first goes through a linear polariser, and then a compensator which gives circular polarization. The light is reflected on or transmitted through the sample, and then goes into a second polariser, which is called an analyser. Finally, light enters a detector. The system measures the change in polarization state of the reflected beam, known as the complex ellipsometric ratio,

$$\tan(\Psi) \cdot e^{i\Delta} = \rho = \frac{r_p}{r_s}, \tag{2.30}$$

where

$$r_p = \frac{E_{rp}}{E_{ip}}. \quad r_s = \frac{E_{rs}}{E_{is}}, \tag{2.31}$$

are the amplitude reflection coefficients for p-and s-polarized light, respectively, defined by the ratios of reflected (r) and incoming (i) p-and s-polarized electric field components. $\tan \Psi$ is the amplitude ratio of the electric field components, Δ is the phase difference between them. Thus, ellipsometry has several advantages over other techniques where intensity is the only measurement, as a function of wavelength;

- Ellipsometry measures at least two parameters for each wavelength

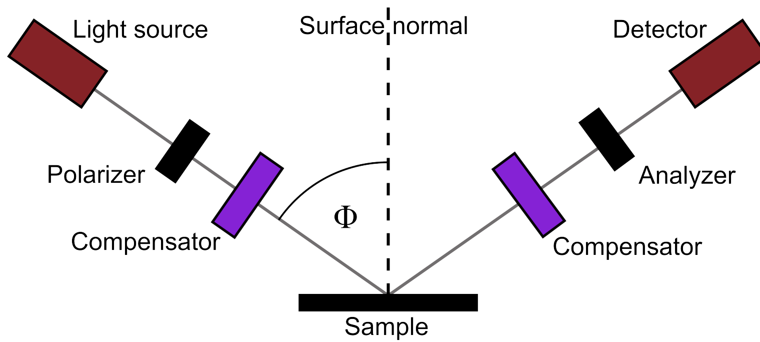

Figure 2.19: Schematic of an ellipsometry setup

- It measures intensity ratios rather than absolute intensities, so it is less affected by instabilities.

- Ambient unpolarized light will not significantly affect the measurement since polarized light is used

- A reference measurement is not necessary

- The entire dielectric function of a material can be extracted.

A drawback of the technique is that it is model-dependent, meaning that a mathematical model has to be constructed and fitted to experimental data to enable extraction of optical, physical and electrical parameters. The ellipsometric ratio can be used to calculate the effective complex dielectric function of a layered sample (such as a thin film on a substrate). Then the parameters have to be extracted with a model using known optical constants of the substrate and a dispersion relation. This calculated optical response is then fitted to the measured response by varying the dispersion relation.

Thickness of optically thin film

An optical system consisting of an ambient, a thin film and a substrate, as in the case of a piece of silicon with a native oxide layer, is illustrated in figure 2.20.

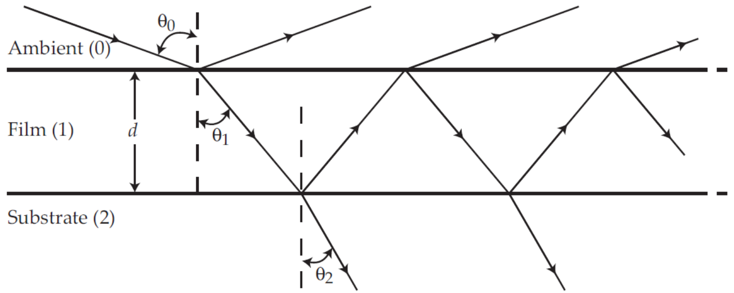

Figure 2.20: Schematic of an ambient-thin film-substrate system [53].

When a light wave is incident upon the thin film (coming from the ambient), at an angle θ_0 from the film surface normal, part of the wave is reflected at the same angle, and part of it is transmitted through the thin film, at an angle θ_1 to the surface normal. The same applies for the film and the substrate and the angles θ_1 and θ_2. There is a phase delay between waves reflected at the film surface and waves transmitted through the thin film which go back out into the ambient, which depends on both the film thickness and its index of recfraction. Thus it is possible, by fitting a model of the layered system to acquired data, to extract these values. If either one of them is known beforehand, it may be used in the model to find the other.

Chapter 3

Experimental Details

3.1 Lab and cleanroom use

The deposition experiments were performed in a designated PLD-lab. Much of the other other work was done in NTNU's Nanolab, which is a cleanroom facility divided into parts of different cleanroom classes in compliance with ISO 14644-1 Cleanroom Standards [54]. Table 3.1 gives an overview of where the different types of work was done. All labs are situated at NTNU Gløshaugen, and can be accessed through the same building.

Table 3.1: Overview of lab use.

Work description	**lab used**
Sample preparation	PLD lab
Sample HF etching	Nanolab, cleanroom class 100
Film deposition	PLD lab
Ellipsometry	Ellipsometry lab, physics department
X-ray diffraction	XRD lab, material sciences department
S(T)EM	Nanolab, cleanroom class 10000
Sputtering/e-beam film deposition	Nanolab, cleanroom class 100
Wafer scribing	Nanolab, not cleanroom

3.2 Pulsed Laser Deposition system

A sketch of the PLD system used in this work is shown in figure 3.1. It is a load locked system which also has a RHEED gun and phosphorescent screen mounted on it (not shown in figure), which are mounted from top to bottom. The system has a base pressure lower than $1 \cdot 10^{-7}$ mbar.

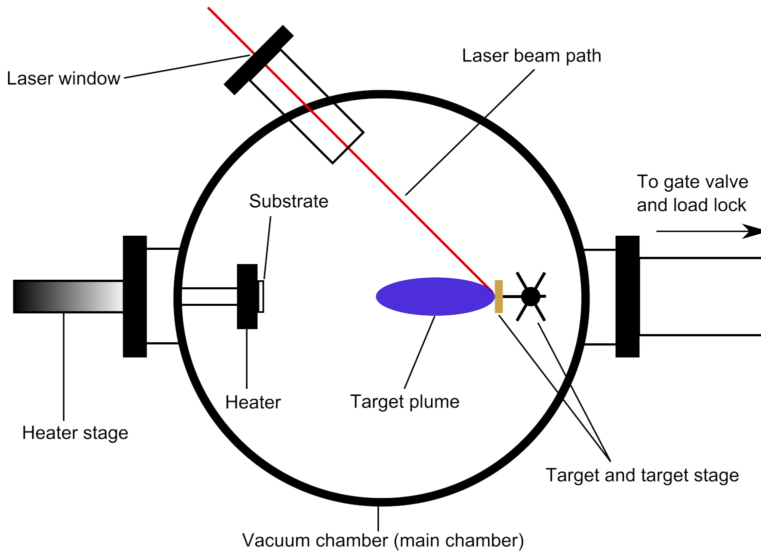

Figure 3.1: Top view schematic of the PLD setup used in this work. RHEED gun and phosphorescent screen with mounted camera which are not shown here, are situated on top and at the bottom of the chamber, respectively, towards the middle of the chamber.

3.2.1 KrF Excimer Laser

The laser used in this work is a Compex Pro 248 nm UV excimer laser. The term "excimer" stems from "excited dimer"; a dimer is a diatomic molecule. This terminology is somehow incorrect in the case of a KrF laser since there is no dimer. (It stuck around due to the first excimer lasers working with diatomic xenon). A better suited term would be "exciplex", from "excited complex". Exciplex lasers are gas lasers, which work by exciting inert gases by laser pumping. In the case of a KrF laser, the overall process can be described by equation 3.1. The asterisk indicates an excited state.

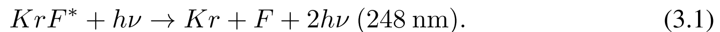

$$KrF^{*} + h\nu \rightarrow Kr + F + 2h\nu\ (248\,\mathrm{nm}). \tag{3.1}$$

A schematic of the laser beam path is shown in figure 3.2. The beam and all the optics are inside a plexiglass enclosure, to avoid risk of exposure to UV radiation. In addition, UV resistant goggles are used at any time the laser is running.

3.2.2 Laser spot

A optical microscope image of the laser spot on the target is shown in figure 3.3. The path length from the laser to the lens and from the lens to the target are such that the laser beam is imaged (and not focused) onto the target, for a more uniform energy density distribution

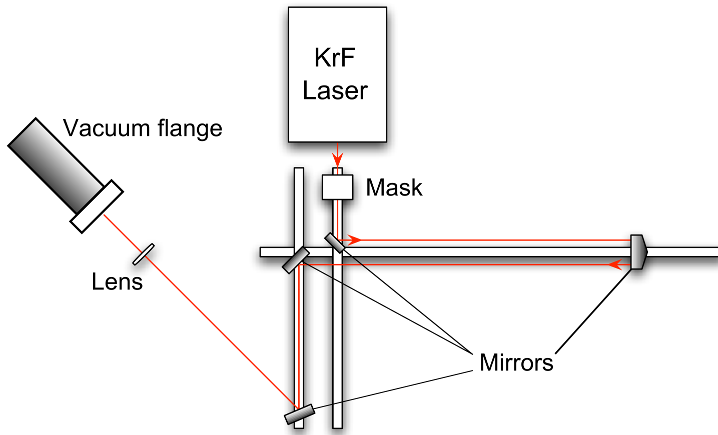

Figure 3.2: Schematic of the laser beam path. The red line shows the beam path. The mirror to the far right can slide along the direction parallel to the beam, to adjust the beam path length. A 5x15 mm mask is placed close to the beam exit.

[55]. Also, a 5x15 mm metal mask is placed near the beam exit from the laser, to have a better defined beam.

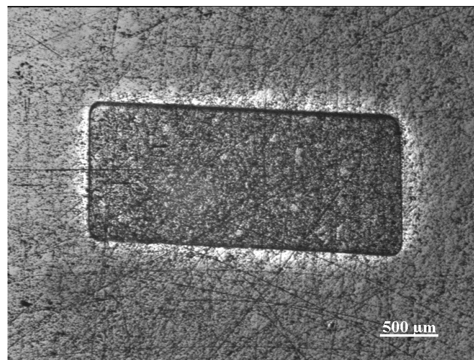

Figure 3.3: Black and white microscope image of the laser spot on the target. The spot looks uniform and the edges are sharp. Its dimensions are approximately $1.97 \times 0.97\ \mathrm{mm}^2$.

3.2.3 Energy measurements

The laser pulse energy was measured with a ThorLabs ES245C pyroelectric energy sensor with a resolution of 1 μJ and an uncertainty of $\pm 5\%$, connected to a computer. The power meter was placed between the last mirror and the lens, due to convenience. The pulse energy is usually measured by averaging at least 30 pulses. The lens transmission was

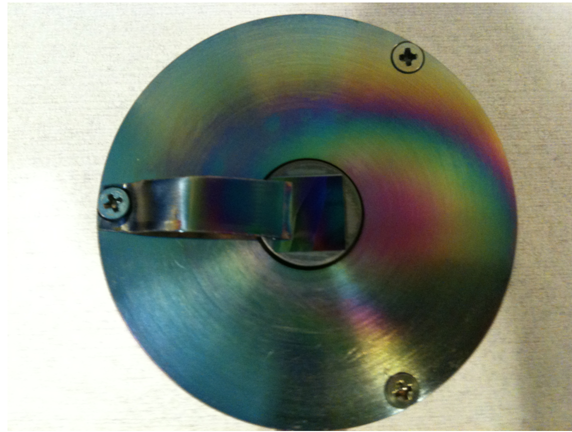

Figure 3.4: Picture of the heater with a sample, after deposition. Notice the different colors due to interference fringes, and the elliptical shape of the plume on the heater and sample.

measured to be 90% and the laser window transmission was measured each time it was removed and cleaned. This is necessary due to contamination on the inside of the window during deposition, which reduces the actual laser fluence on the target.

3.2.4 Substrate mounting and heater

The heater used is pictured in figure 3.4. The sample is held in place with a clamp made of Tantalum, which is fastened with a screw onto the edge of the heater. Between every deposition, the heater surface and clamp are grindedusing conventional grinding paper, so as to remove most of the previously deposited material and to have starting conditions as identical as possible for each deposition.

3.2.5 Substrates

All the Si (100) substrates are from Boron doped p-type silicon wafers of thickness $525 \pm 25\,\mu\mathrm{m}$ supplied by Si-Mat Silicon Materials. The resistivity is $1 - 30\,\Omega\mathrm{cm}$. The substrates were either cut with a manual scriber or with a Dynatex DX-III combined scriber and breaker with a diamond tip scriber and an impulse bar breaker.

3.2.6 ZnS Target

The ceramic ZnS target used is a square $25 \times 25 \times 5\ \mathrm{mm}^3$ with density $3.66\ \mathrm{g/cm}^3$ and purity 99.99%, supplied by the Kurt J. Lesker Company. It is produced by pressing and sintering ZnS powder. This is a suitable target for PLD since it is dense and flat, enabling

uniform energy transfer to its surface, and the absence of voids keeps large particles from being ejected from the surface.

3.2.7 General deposition procedure

The following list gives the general procedure followed for all thin film depositions in this work.

- In the evening, the target is grinded and put into the loadlock.
- The day after, the target is transferred to the main chamber.
- The laser is set for the desired energy, and the energy is measured.
- The target is preablated in an argon atmosphere.
- The substrate is prepared and loaded into the loadlock. To have a good base pressure, I usually waited at least an hour before loading the sample into the main chamber.
- The substrate is heated to the desired temperature before deposition.
- When the desired temperature is reached, argon is again set to flow into the chamber, and deposition is started.

For some depositions, only half the area of the target was used, so that it was not necessary to remove it and polish it before the next deposition, but only preablation was done.

3.3 Substrate preparation

The ”house” clean

The substrate preparation procedure for silicon which has been developed by a previous phd student in the department (which I will refer to as the ”house clean”), is as follows:

1. 7 minutes cleaning in acetone in an ultrasonic bath.
2. 7 minutes cleaning in isopropyl alcohol (IPA) in an ultrasonic bath.
3. 7 minutes rinsing in De-Ionised Water (DIW) in an ultrasonic bath.
4. 3 minutes etching in 5% hydrofluoric (HF) acid (aqueous solution).
5. 3 minutes rinsing in running DIW.
6. substrate is mounted on heater and loaded to load lock.

7. Before deposition, the substrate is heated to $850\,^{\circ}\mathrm{C}$ to remove the hydrogen passivation from the surface.

The purpose of HF etching is to remove the oxide layer which covers any silicon substrate exposed to air for some time. It should also passivate the surface with hydrogen atoms, to keep the surface non-reactive until deposition. After the substrate has been loaded into the vacuum chamber, heating the substrate to $850\,^{\circ}\mathrm{C}$ for two minutes should remove the hydrogen passivation and make the substrate clean and ready for deposition. The acetone and isopropanol are of purity $>$99.8%.

3.4 Experiments

Common to all ZnS thin films depositions is that the laser frequency is $5\ \mathrm{Hz}$, the fluence is about $2.8\ \mathrm{J/cm^2}$, and the target-to-substrate distance is $65\ \mathrm{mm}$. The fluence takes into account the 90% transmission of the lens and the transmission of the window, which is cleaned and measured before each deposition or series of depositions. The fluence may thus be slightly lower in a second experiment without window cleaning, but with the background pressure used during deposition, this was found to be only an insignificant amount. The reason for the decrease in fluence is contamination of the laser window from the target material.

3.4.1 Substrate temperature

Due to the differences in temperature between the substrate and the temperature set by the heater, the substrate temperature is usually measured right before deposition, using an infrared pyrometer through one of the chamber windows, aiming at the central area of the substrate.

3.4.2 ZnS Target

X-ray diffraction using a Bragg-Brentano geometry was performed on the target, to see what phases of ZnS are present in it. EDS analysis was also performed, to find the ratio of zinc to sulfur in the target.

3.4.3 ZnS thin film growth on silicon (100) and (111) substrates

To compare the growth of ZnS thin films on silicon substrates of different orientations, pieces of (100) and (111) silicon were prepared simultaneously, and deposited on simultaneously. Table 3.2 gives the parameters for these experiments. Alle these samples were prepared according to the "house clean" and heated to $850\,^{\circ}\mathrm{C}$ before deposition.

Table 3.2: Deposition conditions for films grown on silicon (100) and (111) simultaneously. Samples with ID starting with the same number are grown simultaneously.

Sample ID / substrate orientation	Heater set T (°C)	Measured T (°C)	Laser Fluence ($\mathrm{J/cm^2}$)	Ar pressure (mbar)	# of pulses
130611A (100)	650	545	2.8	$3.0 \cdot 10^{-3}$	16000
130611B (111)	650	560	2.8	$3.0 \cdot 10^{-3}$	16000
130612A (100)	630	550	2.8	$3.0 \cdot 10^{-3}$	16000
130612B (111)	630	590	2.8	$3.0 \cdot 10^{-3}$	16000

3.4.4 Etched and unetched Si (100) susbtrates

To see whether the etching of substrates in HF acid before deposition has any evident effect on the growth morphology and/or crystal orientation and structure of a deposited ZnS thin film, samples were made under near identical conditions, and prepared according to the "house clean" described in section 3.3, with steps 4 and 5 (HF etch and DIW rinse) ommited for one sample. Table 3.3 shows deposition parameters for these samples.

Table 3.3: Deposition conditions for ZnS films grown on etched and unetched silicon (100).

Sample ID	Etched	Heater set T (°C)	Measured T (°C)	Laser Fluence (°C)	Ar pressure (mbar)	# of pulses
130611A	Yes	650	545	2.8	$3.0 \cdot 10^{-3}$	16000
140128	No	570	545	2.8	$2.8 \cdot 10^{-3}$	12000

3.4.5 In-situ oxide removal and ZnS film growth

I. P. McClean et. al. [56] reported growth of single crystal ZnS on Si (100) by RF magnetron sputtering (RFMS) as well as by MBE, where the substrate preparation involveed

no chemical treatment or etching. Instead, the native oxide on silicon was removed by sputtering at higher temperature. For the RFMS samples, the process was as follows;

- Load a clean 4 inch n+ Si (100) wafer into the chamber
- Slowly increase temperature to $700\,^{\circ}\mathrm{C}$.
- When temperature has stabilized, a 99.98% pure ZnS target is set to sputter at the Si surface with an argon pressure of $2 \cdot 10^{-3}$ mbar.
- After 30 minutes, the Si temperature is decreased to $250\,^{\circ}\mathrm{C}$ while sputtering is continued.

A similar process was used for growth in the MBE system. In-situ RHEED was used to monitor the growth in the MBE system, and the removal of the oxide at $700\,^{\circ}\mathrm{C}$ could be seen as a RHEED pattern corresponding to a Si (100) surface after about 20 minutes. This pattern also remained as the substrate temperature was lowered, indicating that there was no reoxidation.

Although film growth and species dynamics in a PLD system can be very different from both RFMS and MBE, a similar procedure as the one described above for the RFMS was tested in the PLD system. The temperature range, the base pressure and the argon pressure used during growth are similar to common operating conditions in our PLD system. However, our previous experience with ZnS films on Si, suggest that better films are obtained around $500 - 550\,^{\circ}\mathrm{C}$, so growth temperatures were varied from $500\,^{\circ}\mathrm{C}$ to $400\,^{\circ}\mathrm{C}$ for these samples. The samples were cleaned but not etched before deposition. The target was preablated with 2000 pulses before each deposition. 3 samples were made at temperatures starting at 700 and ending at 550, 500, and 400 °C. The argon pressure during deposition was about $2.8 \cdot 10^{-3}$ mbar and the samples were heated to $700\,^{\circ}\mathrm{C}$ at $10\,^{\circ}\mathrm{C/min}$. Then, the laser was set to impinge on the target for 30 minutes at 5 Hz (9000 pulses), before the temperature was lowered to deposition temperature, with the laser still on. The total number of pulses was 20000.

3.4.6 ZnS thin film growth on coated Si(100) substrates

The effect of ZnS film growth was investigated on Si (100) substrates coated with thin layers of Au, Al and Ge. The main purpose of this experiment was to substantiate the observation that ZnS thin films often have a [111] preferred orientation, regardless of what they are grown on, under similar conditions as previous experiments. These buffer layers were deposited using an AJA Sputter and Evaporator Custom ATC-2200V model by AJA International Inc., in the NTNU Nanolab. Three identical silicon 10x10 mm pieces were sputtered in an Ar plasma for 5 minutes before thin films less than 5 nm thick were deposited. One element was deposited on each substrate. The three samples were loaded

together to the PLD system and heated to $550\,^{\circ}\mathrm{C}$. ZnS films were deposited with 12000 pulses and an Ar backgrond pressure of $3 \cdot 10^{-3}$ mbar. A heater with a larger heated area was used for this experiment to be able to put three samples at the same time. Each sample was held in place by separate clamps.

3.4.7 HF etching and ellipsometry measurements

The 3 minutes of etching in 5% HF in the "house clean" supposedly removes the native oxide covering the silicon wafer and passivates its surface with atomic hydrogen. However, after etching, the substrate is transported in air, and it usually takes about 20 minutes to get the sample into the load lock of the vacuum system, due to the HF bench being in another part of the building. Ellipsometry measurements before and after etching can give precise data (sub-Ångstrøm accuracy) on the thickness of the oxide layer, before and after etching, and can also establish the time evolution of the reoxidation of the surface after etching.

Instrumentation

The ellipsometry used in this work is a J. A. Wollam Co., Inc Ellipsometry Solutions RC2 ellipsometer. Standard ellipsometry measurements were done at a fixed angle of 65° and acquisition time was 40 seconds. The instrument is a complete Mueller matrix system based on two rotating retarders. The illumination part consists of a 150 W Xe lamp with a source pin-hole of 100 m and collimation optics giving an initial beam waist diameter of approximately 3 mm. The detection system consists of a combination of an InGaAs and a Si spectrograph, where the data are recorded at wavelengths from 210 to 1700 nm (0.73 to 5.9 eV) with a resolution of 2 nm for wavelengths $>$1000 nm, and 1 nm for wavelengths $<$1000 nm.

The model used is a three-layer model with silicon, and interface layer which is a mixture of silicon and silicon dioxide, and a silicon dioxide layer on top of that. The indices of refraction from these layers are taken from the database supplied with the software that comes with the instrument.

Procedure

10 x 10 mm pieces of silicon (100) were cleaned according to the "house clean". After the 3 min etch in 5% HF, they were rinsed for 3 minutes in DI water and transported as quickly as possible, in air, to the ellipsometry lab, in a plastic box. The time between the etching and the start of the ellipsometry measurement was about 13 minutes. One measurement was set to last 40 seconds, with measurements every 10 minutes. The measurements were set to run overnight, that is, for more than 15 hours. During the measurements, the sample is in air.

3.4.8 Cleaned Si and RHEED imaging

A 10x10 mm piece of Si was cleaned according to the house clean, and loaded to the main chamber. It was heated gradually, whit the RHEED setup set to impinge along the [110] direction of the crystal. The purpose was to be able to see and recognize the characteristic RHEED pattern which emerges when a silicon (100) surface goes from a 1x1 into a 2x1 reconstruction, as discussed in chapter 2. The substrate was first heated to 600 °C, then gradually up to 800 °C. The electron gun is operated at voltages around $12 - 20$ kV and currents around 1.4 A.

3.5 Characterization

3.5.1 Film Thickness

The profilometer used to determine film thickness is a Dektak 150 from Veeco, which is a contact stylus profilometer. It has a 12.5 µm diamond tip stylus which runs over a sample surface, and the recordings are sent directly to a computer with proprietary software. The height range of the instrument can be varied. Since the films grown in this work are less than a µm thick, the lowest range of 6.55 µm is employed. Using this range, the instrument has a best vertical resolution of 1 Å.

Since a clamp covers part of the substrate during deposition, there is a sharp transition between the film and the substrate, making thickness measurements easier. To estimate the thickness of the film, two points on the lower side (where there is no film) are leveled, and if the surface of the film appears relatively flat, the step height is taken as a value for the thickness. For each film, several measurements are performed, and the average value is calculated. These values are also compared with values from cross section SEM imaging for reference.

3.5.2 X-ray diffraction and GIXRD

The apparatus used for X-ray diffraction is a Bruker D8 Advance diffractometer equipped with a $\mathrm{Cu - K_{\alpha}}$ radiation source and LynxEye XE detector. For XRD of the ZnS target, a Bragg-Brentano geometry is used. For the thin films, the instrument is equipped with parallel beam optics, (Goebel mirror plus 0.2 degree receiving slits), and data are collected in grazing incidence mode with a fixed incidence angle of 1 degree. The sample is rotated during the scan.

3.5.3 SEM

Hitachi S-5500

The first microscope used in this work is a Hitachi S-5500 S(T)EM, placed in an electromagnetic field-free room on vibration-isolateed ground. It has detectors for secondary and low- and high-angle back scattered electrons, bright-field and dark-field transmission measurements and a Bruker XFlash EDX Detector. Since the S-5500 is an in-lens cold field emission electron microscope the achievable resolution with is down to 0.4 nm. However, this resolution strongly varies with the sample. Parameters such as voltage, current and scale can be seen in each picture presented. This microscope is used for everything except EDS measurements on the target.

Sample preparation

The S-5500 SEM has a sample size limit of $5 \times 9 \times 3\,\mathrm{mm}$ (W × L × H). Since the samples originally are larger than this, small pieces are broken of manually with a hand scriber.

Hitachi TM 3000 tabletop SEM

This instrument is an easy-to use and quick compact SEM with a BSE and EDS detectors. For EDS analysis, it operates at $15\,\mathrm{kV}$.

3.5.4 RHEED

The RHEED system is a STAIB Instrumente high pressure RH30 with a tungsten filament. It is usually operated at voltages from 12-20 kV and at a filament current of about $1.4\,\mathrm{A}$.

Chapter 4

Results

4.1 Penetration depth of X-rays in ZnS

For cubic zinc sulfide, with a lattice constant of 4.52 Å, the electron density is $1.156\ \text{Å}^{-3}$, and the aborption coefficient is $31.7\,\mathrm{mm}^{-2}$ [17, Chapter 2]. This gives $\delta = 7.98746 \cdot 10^{-6}$ and

$$\alpha_c = \arccos(1 - 7.98746 \cdot 10^{-6}) = 0.229°. \tag{4.1}$$

The calculated penetration depth using equation 2.13, as a function of incidence angle, for cubic zinc sulfide is shown in figure 4.1. The plot can be used as a starting point for what incidence angles should be used in GIXRD.

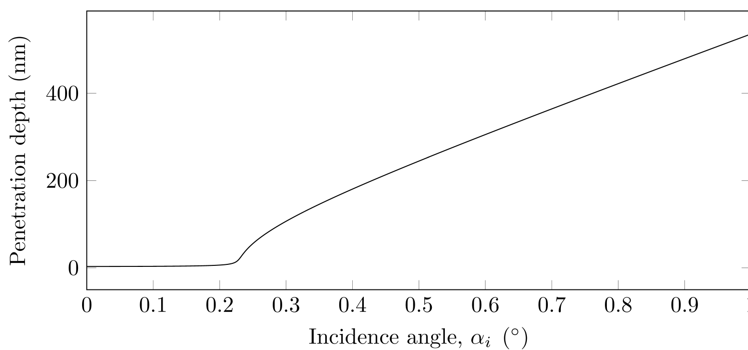

Figure 4.1: Theoretical penetration depth of Cu $k_{\alpha 1}$ as a function of incidence angle for cubic zinc sulfide

4.2 ZnS target

X-ray diffraction

X-ray diffraction from the ceramic ZnS target using a standard Bragg-Brentano geometry is shown in figure 4.2. The peaks match well with the JCPDF-01-071-5976 for zinc blende ZnS, but there are also visible wurtzite peaks.

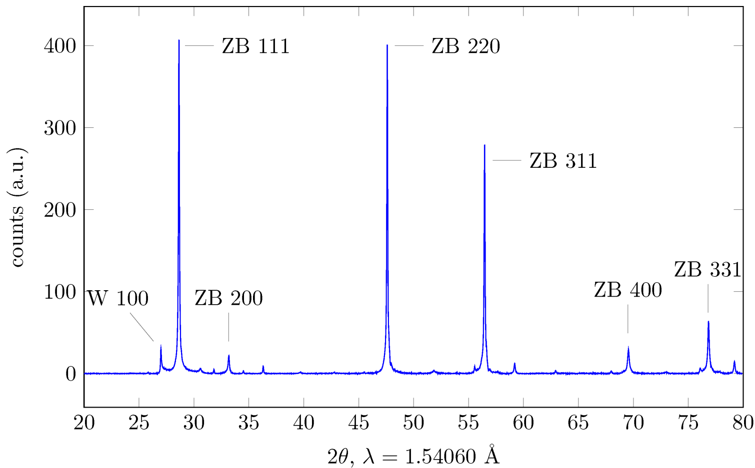

Figure 4.2: XRD data from the ceramic ZnS target. Zinc blende and wurtzite peaks are indicated by ZB and W, respectively.

EDS

EDS data was collected from the ZnS target at three different locations. A quantifying procedure using an interactive PB-ZAF model was used to determine the ratio of zinc to sulfur. The average of these measurements, neglecting elements other than zinc and sulfur (such as carbon and oxygen present on the surface)s, give an average of 54.3% sulfur and 45.7% zinc, indicating that the target is sulfur-rich.

4.3 ZnS thin films on Si (100) and (111) substrates

Results for the samples described in section 3.4.3 are presented here. Thicknesses as measured by profilometer and substrate temperatures as measured by pyrometer before deposition for the films are shown in table 4.1.

Table 4.1: Thicknesses and growth temperatures of films grown on silicon (100) and (111).

Sample ID (substrate orientation)	Film thickness (nm)	substrate temp. (°C)
130611A (100)	540	545
130611B (111)	555	560
130612A (100)	555	550
130612B (111)	480	590

Sample 130612B stands out as the thinnest film, and has the highest measured growth temperature. Figures 4.3 and 4.4 shows GIXRD data for the two sets of samples grown simultaneously.The dominant peak is identified as the ZB(111)/W(002) peak in both cases, but the W(103) peak is also present. The data is shifted along the y-axis for good visibility, and samples grown simultaneously are plotted with the same color. Figure 4.5 shows SEM cross section images of the same samples. The contrast between the substrate and the films is good, and the substrate appears black in the lower region of the images. The images show that the films on substrates of different orientation are distinctly different. Figure 4.7 shows the surfaces of the films, also revealing a distinct difference in the surface morphology for the two different substrate orientations. Figure 4.6 reveals the grains structure at the interface.

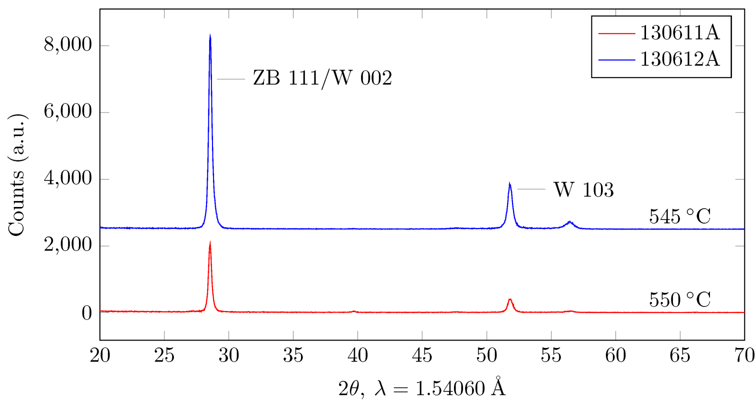

Figure 4.3: GIXRD data from ZnS films on silicon (100).

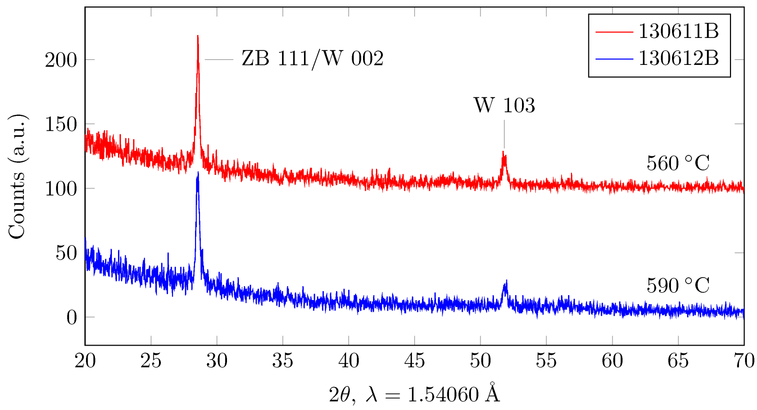

Figure 4.4: GIXRD data from ZnS films on silicon (100).

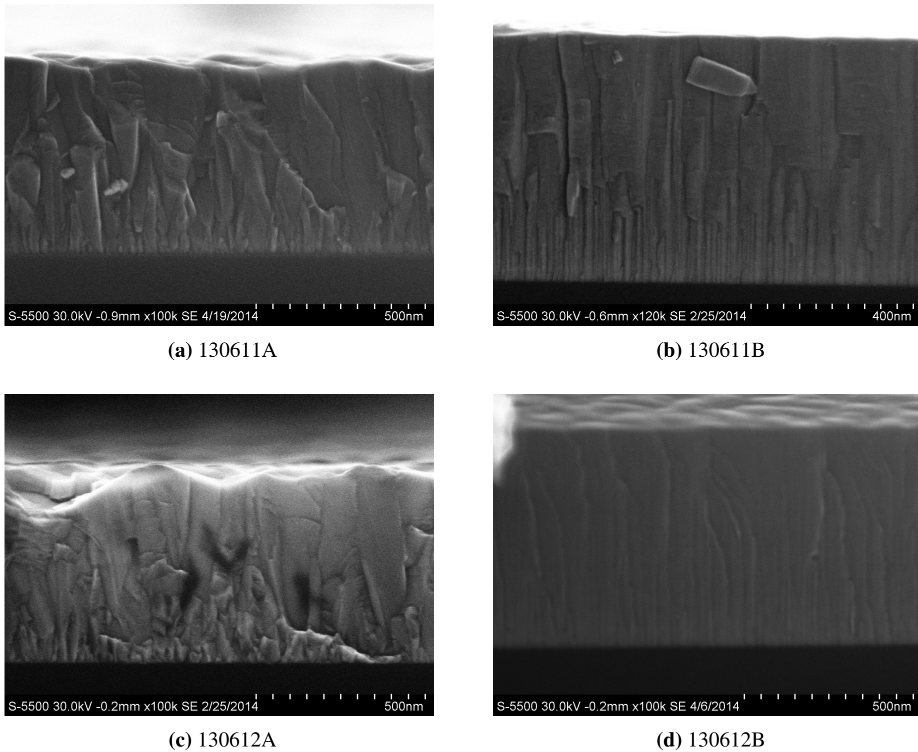

(a) 130611A

(b) 130611B

(c) 130612A

(d) 130612B

Figure 4.5: SEM cross section images of thin films on silicon (100), (a) and (c) and on silicon (111), (b) and (d). Images (a), (c) and (d) are taken at x100k magnification, and image (b) at x120k magnification. All images are taken with an acceleration voltage of 30 kV.

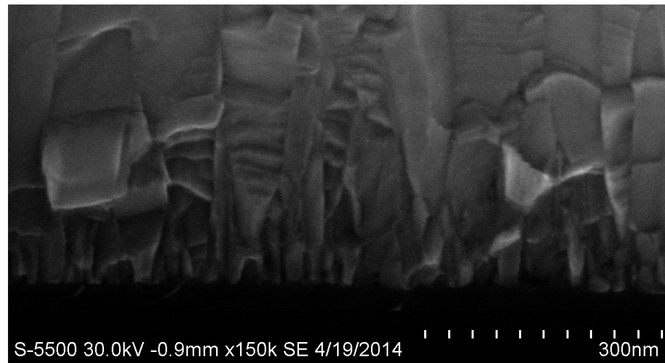

Figure 4.6: Close-up SEM image of the interface of sample 130611A. Notice how the grains get smaller at towards the interface.

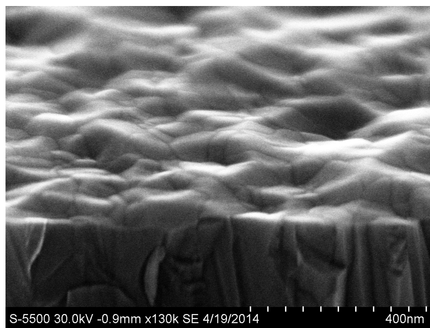

(a) 130611A

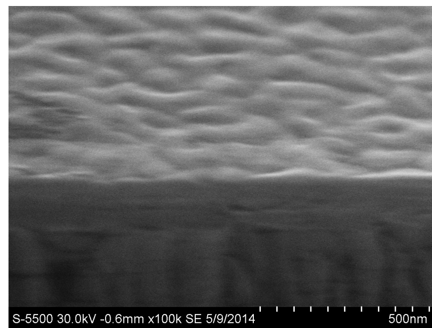

(b) 130611B

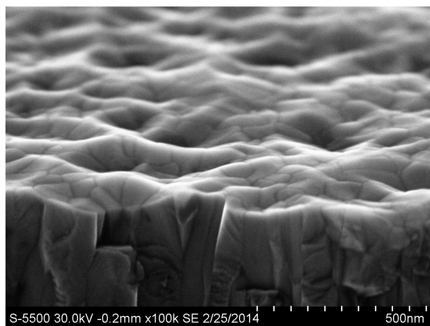

(c) 130612A

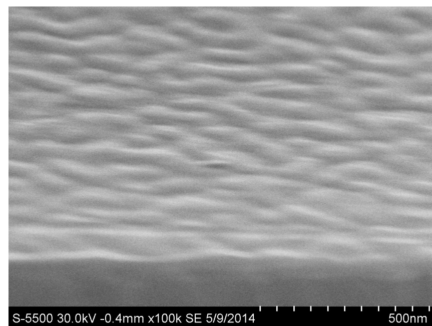

(d) 130612B

Figure 4.7: SEM images of the sample surfaces, seen from the side. (a) and (c) are films on silicon (100), (b) and (d) are on silicon (111). (a) is taken with x130k magnification, and the other three at x100k magnification.

4.4 ZnS films on etched and unetched (100) silicon substrates

This section presents the results for the samples described in section 3.4.4. The GIXRD data from samples 130611A (etched substrate) and 140128 (unetched substrate) are presented in figure 4.8. The main peaks are identified as the ZB(111)/W(002) and the W(103) peaks. These are the same for both samples, although the peaks are much stronger for the film on an ethced susbtrate. The thickness of the films were found to be 540 nm and 430 nm, respectively. SEM images of the samples are shown in figure 4.9. The images reveal similar cross sectional and surface features.

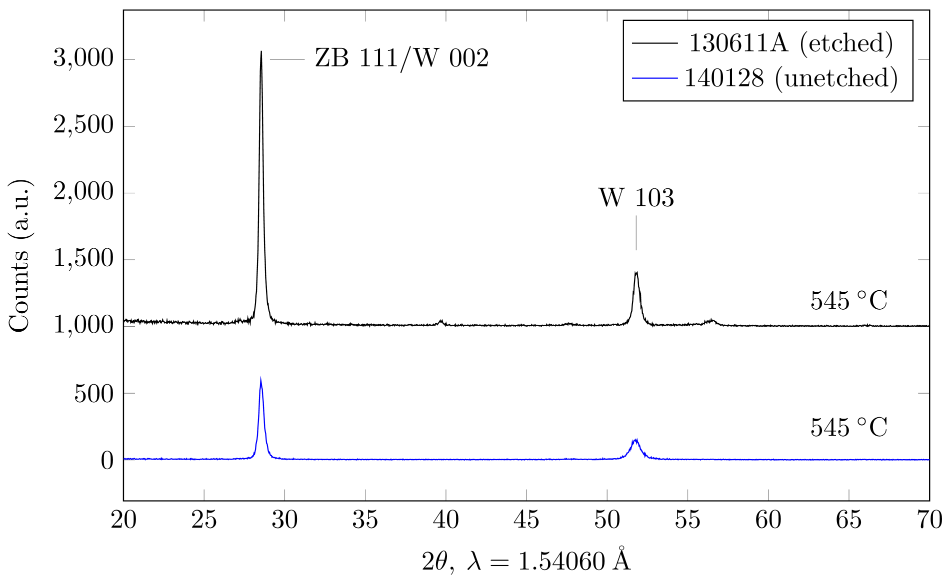

Figure 4.8: GIXRD data from samples 130611A (etched silicon (100)) and 140128 (unetched silicon (100)). The peak at around $2\theta = 28.5°$ is the zinc blende 111 peak and/or the wurtzite 002 peak. The smaller peak on the right side around $2\theta = 52°$ is the wurtzite 103 peak.

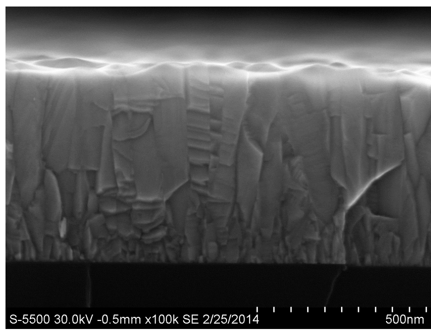

(a) 130611A

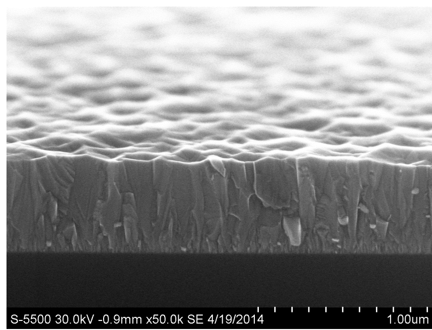

(b) 130611A

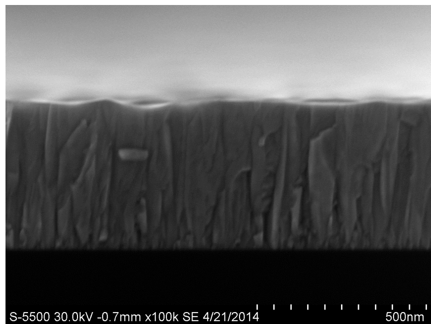

(c) 140128

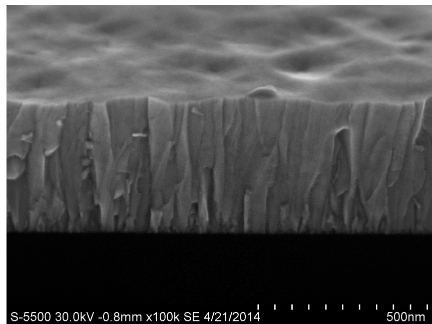

(d) 140128

Figure 4.9: SEM cross section images of samples 130611A (etched silicon (100)) and 140128 (unetched silicon (100)). The top surface of the films is visible in figures (c) and (d) since the sample is tilted.

4.5 In-situ oxide removal and ZnS film growth

Presented here are results for the films grown as described in section 3.4.5. Profilometry measurements showed that the film, in some of the samples, was buried beneath the substrate surface. Therefore, the difference in height between the substrate and the film (h) was measured by profilometer, and the film thickness (d) was measured in cross section SEM images. The amount of removed silicon is thus d+h Table 4.2 shows the results. Figure 4.10 shows the GIXRD data for the samples. The dominant peak in all three samples is the ZB(111)/W(002) peak, as in previous samples. The other significant peak is the ZB(311)/W(112) peak. The former peak decreases with temperature, whereas the latter slightly increases.

Table 4.2: Data on films grown by in-situ oxide removal and subsequent ZnS film growth.

Sample ID	growth T. (°C)	film-substrate height, h (nm)	film thickness, d (nm)	Amount of removed silicon, d+h (nm)
140213	700-550	-90	140	230
140214	700-500	-70	115	185
140216	700-400	35	200	165

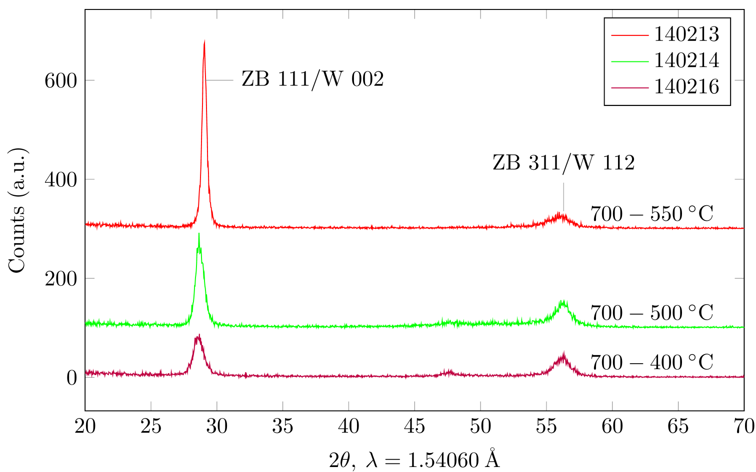

Figure 4.10: GIXRD data for samples grown by in-situ oxide removal and subsequent ZnS film growth. The temperature range at which the films are grown is indicated.

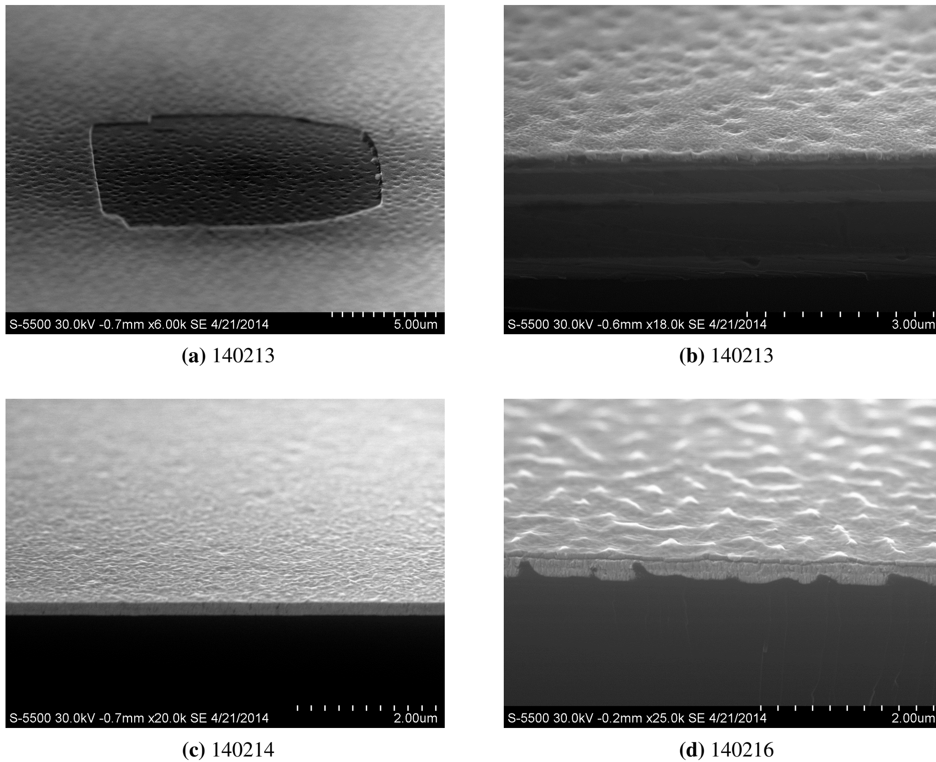

(a) 140213 **(b)** 140213

(c) 140214 **(d)** 140216

Figure 4.11: SEM images of samples grown by after in-situ oxide removal. In figure (a), part of the film has come off the substrate, hence the darker region in the middle. (a) and (b) show the same sample grown at highest temperature, (c) and (d) show the two other samples grown at lower temperatures.

4.6 ZnS thin film growth on coated Si(100) substrates

Figure 4.3 gives the thickness of the ZnS films grown at 550 °C on coated susbtrates as described in section 3.4.6. The first two films grown on Al (140303Al) and Au (140303Au) have similar thicknesses, and the one grown on Ge (140303Ge) is significantly thicker. GIXRD data from these samples is shown in figure 4.12. Again, the dominant peak is the ZB(111)/W(002) peak, with the W(103) peak also present.

Table 4.3: Thickness of films grown simultaneously on coated silicon (100).

Sample ID	Film thickness (nm)
140303Al	170
140303Au	175
140303Ge	215

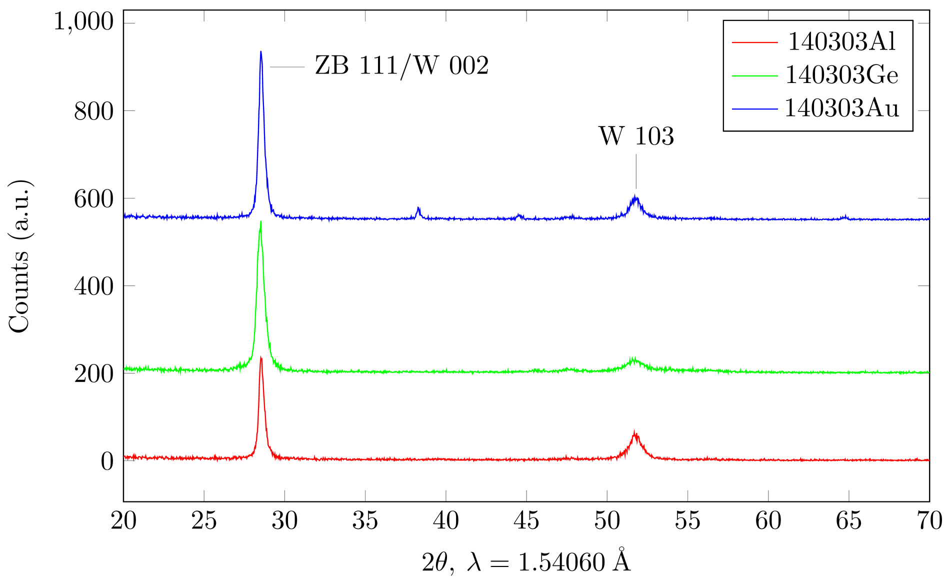

Figure 4.12: GIXRD data from ZnS films grown on coated silicon (100) substrates.

4.7 Ellipsometry on etched Si(100) substrates

Ellipsometry measurements and modeling was performed by Zahra Ghadyani at the applied physics group at the department of physics, NTNU. The thickness of the interface and oxide layer (meaning the sum) before etching was found to be 1.74 nm by a single ellipsometry measurement. Figure 4.13 gives the time evolution of the reoxidation of a piece of silicon (100), after it was cleaned and etched with the procedure described in section 3.4.7. The experiment was repeated, and near identical results were obtained. The same experiment was also done with a much shorter rinsing time in DIW after etching. This also gave almost identical results. The measured oxide thickness at the start of the measurement is about 0.7 nm, and the thickness gradually increases at a decreasing rate.

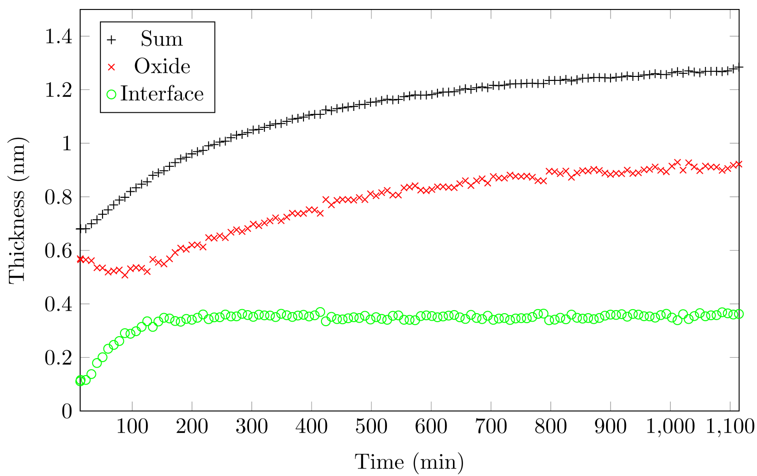

Figure 4.13: Thickness of interface and oxide (green and red) as a function of time on Si (100) etched for 3 min. in 5% HF, as measured by ellipsometry. The measurements started about 13 min. after the etching. The black crosses shows the total thickness of the two layers.

4.8 Cleaned Si and RHEED imaging

Figure 4.14 shows RHEED images taken after cleaning, etching and heating a piece of silicon (100) as described in section 3.4.8. The diffraction pattern from an unetched substrate in figure 4.14 (a) is diffuse, in contrast to figures (b) and (c), which show much sharper features, although not sharp as bright as in figure **??** of section 3.4.8. The 2x1 reconstruction dots are visible in figure (c), but they are very faint and diffuse. The contrast-ajusted image of figure 4.14 (c) is shown in figure 4.14 (d), making the 2x1 diffraction spots much more visible.

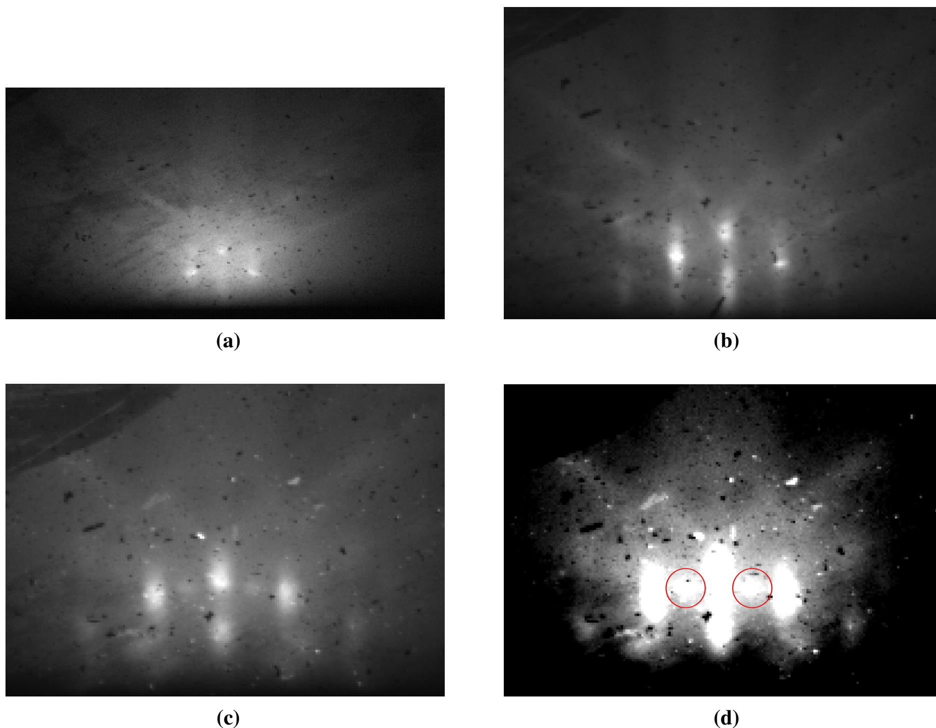

(a) **(b)** **(c)** **(d)**

Figure 4.14: RHEED patterns from cleaned and heated silicon (100) with electron beam incident along the [110] direction at an acceleration voltage of 12 kV. (a) Shows an unetched substrate at room temperature, for comparison. (b) is after 1 hour at 600 °C, (c) is after two hours, and after about 30 minutes at 800 °C. (d) is the same image as (c), but with ajusted contrast, so the 2x1 diffraction spots are visible (red circles).

Chapter 5

Discussion

5.1 General Remarks

5.1.1 Diffraction peaks

The GIXRD data collected from the samples, shows that all the films are strongly oriented, because of the prevalence of some peaks, and the absence of others. The data thus cannot be used very much for quantitative analysis as in powder diffraction. The preferred orientation results in relative peak intensities being very different from a reference powder sample where all orientations are assumed equally probable and the sample isotropic. Some of the zinc blende and wurtzite peaks for ZnS are very close to each other, and since the peaks are relatively broad, both due to grain size and the fact that there is both $K\alpha_1$ and $K\alpha_2$ radiation in the instrument, it is very hard to separate the peaks. Take the zinc blende (111) peak and the wurtzite (002) peaks, for example. They are located at $2\theta = 28.4253$ and $2\theta = 28.4900$, respectively, so the difference is about $0.065°$. On the other hand, the FWHM of any of these peaks from GIXRD data is of order $0.3°$. Unless a sample only shows distinct peaks from either zinc blende or wurtzite which do not overlap with one another, such as the 200 and 400 zinc blende peaks or the 100 wurtzite peak, it is not possible in this analysis to tell if the peak is ZB or W, one can only assume a contribution from both, although they can be discussed in light of the rest of the diffraction pattern. In addition, film thickness and area may vary between samples, affecting the intensity of the peaks. In summary, X-ray data tells if a film is crystalline (if there are sharp peaks), and the most intense peak(s) give information on the orientation.

Substrate peaks

To test wether peaks from the substrate appear during GIXRD scans, a GIXRD scan was done on a piece of silicon (100), with the same scan parameters as for the thin films. No well defined peaks could be observed in this scan. For this reason, it can be said that the significant peaks observed in GIXRD scans of the thin films only come from the thin film itself, and not from the substrate. If the penetration depth of the X-rays should be more than the film thickness, the contribution from the substrate will only be noise.

Powder diffraction files

The peaks from Powder Diffraction Files (PDF) for 00-027-1402 (silicon), 01-071-5976 (cubic ZnS) and 04-008-7254 (wurtzite ZnS), supplied by the International Centre for Diffraction Data, are listed in table 5.1. Note that intensities cannot be compared across the different PDF files, since they are normalized to the highest intensity peak from a reference sample, and the intensity of the highest peak is chosen by convenience.

5.2 ZnS Target

The diffraction pattern from the target is merely shown to get an idea of what diffraction peaks can be expected in the films. Although the target consist of mostly ZB ZnS, this does not tell the structure of the films, since the material is evaporated in transfering from target to substrate.

5.3 ZnS growth on silicon (100) and (111)

In this section, ZnS films grown on silicon (100) and silicon (111) will be referred to as (100) and (111) films, respectively.

GIXRD

The dominant peaks for all four samples are the zinc blende 111/wurtzite 002 peaks, and the wurtzite 103 peaks. Since the ZB 111/W 002 peak is dominant, this indicates the direction of growth, meaning that ZB 111/W 002 planes are parallel to the substrate surface. The peaks from the (100) films are distinctly stronger compared to the ones on silicon (111). Since the W 103 peak is also present, there is no doubt that the wurtzite phase is present in all of the films, since this peak does not overlap with a zinc blende peak. The much higher ZB 111/W 002 peak from the (100) films samples may be due to the presence of a 111-oriented ZB phase which is not seen in the (111) films. This in turn can be understood as the effect of the substrate orientation; Since the silicon (111) surface has a

Table 5.1: Diffraction peaks from Powder Diffraction Files (PDF) 00-027-1402 (silicon), 01-071-5976 (cubic ZnS) and 04-008-7254 (wurtzite ZnS).

$2\theta(^\circ)$	Silicon	Zinc blende ZnS	Wurtzite ZnS	Relative intensity
26.9091	-	-	100	100
28.4253	-	111	-	999
28.4422	111	-	-	100
28.4900	-	-	002	84
30.5201	-	-	101	87
32.9389	-	200	-	86
39.5898	-	-	102	28
47.2733	-	220	-	487
47.3023	220	-	-	55
47.5321	-	-	110	81
51.7384	-	-	103	54
55.4654	-	-	200	11
56.0866	-	311	-	272
56.1205	311	-	-	30
56.3528	-	-	112	47
57.5456	-	-	201	12
58.8184	-	222	-	14
58.9620	-	-	004	2
63.5255	-	-	202	6
65.9629	-	-	104	1
69.0837	-	400	-	49
69.1301	400	-	-	6
72.9296	-	-	203	15
76.3230	-	331	-	68

hexagonal symmetry, it may favor the hexagonal wurtzite structure. The relative intensites of peaks of the films on silicon (111) are close to the ones in table 5.1, thus making it more plausible that the film is wurtzite. In the (100) films, the influence of the substrate on the film breaks down somehow, because the film itself is (111)-oriented, which defeats the purpose of a (100) substrate. The ZB(111)/W(002) peak is much higher, both in absolute value, and relative to the W(103) peak. This is why it is reasonable to discuss that there is a significant contribution from ZB-ZnS in these films, and more so than in the films on silicon(111). One might think that the ZB(222) peak is to be expected if there is contribution from the (111) peak, but the relative intensity of this peak is only 14/1000 of the intensity of the (111) peak. Another issue with this peak is that it lies close to the W (004), which is also to be expected when there is a contribution from the W(002) peak, but this peaks relative intensity is also very low, at 2/84 of the W(002) peak.

Growth and morphology

The effect of substrate orientation is also seen in the SEM images in figure 4.5. In the (100) films, the growth in the first 100 nm or so looks very chaotic and random (figures 4.5 (a) and (c)). This is similar to zone T growth as described in section 2.2.1, where the initial growth consists of grains of many different orientations, and the grains with low surface diffusion grow faster and outgrow the other orientations. The orientations of these grains give the observed preferred orientation in the film. Figure 4.6 shows a high magnification image of the interface between film and substrate of sample 130611A, showing very small grains close to the interface. The grains get bigger as the film grows, but the structure still looks quite random, and the grain boundaries point in various directions, although there seems to be a slight vertical alignment of these boundaries. In terms of growth mode, it is reasonable to say the this is a three-dimensional growth mode.

The cross section images of the films on silicon (111) (figures 4.5 (b) and (d)), reveal something entirely different. Strictly columnar and vertical structures are visible, and there seems to be much more order. The films seem to start with and maintain the same orientation in their entire thickness, and there are no randomly oriented grains competing for growth. There also seems to be a much finer grain structure in the first hundred or so nanometers of the film, and then the grains merge together into bigger grains as the film grows. The high density of the small vertical grains at the interface reflects the inherent high nucleation density in PLD.

Surface features

The surfaces of the (100) and (111) films are shown in figure 4.7. It is clear that these are two completely different surfaces; the (100) films have visible grain boundaries on the surface, and are much rougher than the (111) films. The roughness on the surface can be

due to the effect of competing orientations and shadowing from the faster growing grains, meaning that the grains that grow slower are inside the pits seen on the surface. On the (111) films, the surface appears a lot smoother, and grain boundaries are not visible. The surfaces of these films reflect the effect of the initial growth phase; the (100) films are rough and disordered, the (111) films are smooth and relatively featureless. It seems that these films are of better quality and perhaps of single domain.

5.4 ZnS films on etched and unetched silicon (100) substrates

The GIXRD data in figure 4.8 in section 4.4 shows the same peaks previous samples; the ZB(111)/W(002) and W(103) peaks, which are dominant. This tells that the removal of the native oxide by HF etching does not affect the overall orientation of the film on silicon (100) substrates. However, the peaks from the etched sample are noticeably higher than the ones from the unetched one. This could indicate that the film grown on the etched wafer is more strongly oriented than the other one, meaning that a larger fraction of the grains in the film have this orientation.

The SEM images reveal similar growth morphologies for the two samples (figure 4.9); both the side view cross section images and the surface show similar features.

5.5 In-situ oxide removal and ZnS film growth

The diffraction data presented in figure 4.10 in section 4.5 shows the ZB(111)/W(002) as in other samples, and ZB(311)/W(112) peaks, with a noticeable reduction in intensity and broadening of the ZB(111)/W(002) peak with decreasing growth temperature. The ZB(311)/W(112) peak is low at high temperatures, and increases a bit when growth temperature decreases. For sample 140216, the difference in the height of the ZB(111)/W(002) and the ZB(311)/W(112) peaks is not large. The reduction and broadening of the ZB(111)/W(002) peak can be understood as a reduction of the number of grains with this orientation with decreasing temperature, as well as a decrease in grain size due to lower surface mobility and increased nucleation density. At the same time, the number of grains with a ZB(311)/W(112) orientation increases. This series of samples also demonstrates that the film orientation is slightly sensitive to the temperature variation, for the range of temperatures used, but the dominant orientation is still the ZB(111)/W(002).

The data in table 4.2 is somewhat ambiguous. Since the initial phase with the substrate held at 700 °C is identical for all samples, one would expect the amount of removed silicon to be about the same. This is clearly not the case. Also, the film thickness drops for sample 140214, and then goes up again for sample 140216, grown at a lower temperature. This

behaviour is also unexpected, as film thickness is expected to increase with decreasing temperature, since the mobility of film species is lower and there are less adatoms being reevaporate. It is possible that the heat treatment of the substrate before ablation begins is of importance, and the exact time the substrate is kept at high temperature. The difficulties concerning temperature regulation are adressed in chapter 8.

As can be seen in figures 4.11 (a) and (b), the substrate for sample 140213 has uniformly distributed pits, which are also seen through the film. In figure (d), the substrate is also badly damaged, with what appears to be lobes of silicon extending into the film. In contrast, sample 140214 in figure 4.11 (c), which was grown at $700 - 500\,°\mathrm{C}$, does not immediately reveal the same kind of damage to the substrate and film. Without a precise record of the temperature evolution of the sample, it is hard to say why this is so.

However, the most important aspect of these experiments is the demonstration of the possibility of in-situ removal of material from the surface of the silicon substrate, although the experiment resulted in much more material removed than just the surface layer and that much further work is necessary to develop a procedure which only removes the native oxide from the surface and does not damages the substrate. In this work, the high energy of the impinging species from the target, combined with high temperature and the duration of the procedure, results in the removal of much more material than desired.

5.6 Thin film growth on coated silicon (100) substrates

Figure 4.12 of section 4.6 reveals the same peaks as for the films grown on etched and unetched substrates, and the relative intensities are also similar. The arguments for the preferred orientation of these films are also the same. SEM imaging of these films was difficult, and images are not shown here. However, the determination of orientation was the main purpose of this experiment. Again, this experiment demonstrates the fact that in this work, the ZnS films grown have a preferred orientation that is largely independent of the substrate.

5.7 Ellipsometry measurements on etched silicon substrates

The oxide thickness as showed in figure 4.13 of section 4.7 clearly shows that there is already an oxide layer of about $0.7\ \mathrm{nm}$ on the substrate when the measurement starts after cleaning and etching. The reoxidation is faster for the first 200 minutes or so, and slows down. The reason for the slight decrease in the oxide layer in the first hour or so is unclear; perhaps it is due to a reduction in roughness in the initial oxidation phase, not accounted for in the SE model, or that the model used should be revised with regards to the relation between the interface and the oxide. Nevertheless, the total thickness is really the interesting measure here, and it does not show any unexpected behaviour.

Comparison with literature

The results from these experiments are simlar to the results of Utani and Adachi [57], in that the effective film thickness calculated by spectroscopic ellipsometry does not reach zero after an HF dip. They attribute this to the effect of the adsorbed hydrogen on the surface, and/or the roughening of the surface by HF treatment not accounted for in the SE model. In their paper, Utani and Adachi also compare HF dipping times and the initial oxide thickness as measured by SE. Their cleaning procedure involves rinsing with organic solvents, and then an HF dip in 1.5% aqueous HF followed by a DIW rinse. Their SE data shows that for silicon (100), the measured oxide thickness increases as the HF dipping time increases. At its minimum, it is 9.7 Å (around 25 seconds HF dip). Since in this work, a 5% aqueous HF solution is used, and the dipping time is 3 minutes (180) seconds, it may be that the etching roughens the substrate, and that the HF dipping time is unecessarily long.

Gonda et. al. [58] also did similar experiments, measuring the oxide thickness of silicon (100) and (111) after cleaning and etching. Their results show that for silicon (100), the oxide thickness is about 0.2 nm after etching, and remains close to this value for about three hours. However, their cleaning is different in that they use a pH-modified buffered HF acid, and the final step involves cleaning with $40\%NH_4F$. They also compare SE measurements with X-ray Photoelectron Spectroscopy (XPS) measurements. With XPS, the thickness of the oxide is much closer to 0 after cleaning. In their conclusion, they also attribute the nonzero thickness in SE measurements to the nature of SE (which I interpret as an effect of the model not correctly accounting for roughness or the Si-H bonds, as discussed previously). Apparently, this procedure results in a more stable surface than simply using aqeous HF.

5.8 Cleaned Si and RHEED imaging

The RHEED patterns seen in figure 4.14 (a), a silicon 1x1 reconstruction is visible. After gradual heating to 800 °C, very faint diffraction spots from a 2x1 reconstruction can be seen (figure 4.14 (b)). Multiple experiments were performed with heating for several hours at similar temperatures, but the 2x1 surface reconstruction could not be observed. Although the hydrogen desorption temperature for the 2x1 reconstruction has been reported as 400 °C [59], this is not seen in this work. Since the diffraction pattern in the images is rather diffuse, this indicates that the surface is not clean, and that partial reoxidation has occured. However, the diffraction is still much sharper than diffraction from an unetched piece of silicon (100) as in figure 4.14 (c). Anyhow, the experiments with etched and unetched silicon (100) substrates reveal same orientation films with similar morphologies. It remains to be seen if they have similar electronic properties. Since it has been shown that there can be significant removal of silicon at high temperatures, it is possible

that this also happens in depositions at a couple hundred degrees lower. Therefore it is somewhat uncertain if films grown on substrates that have not been etched, really grow on a layer of silicon oxide, or if this layer is removed in the beginning of a deposition.

5.9 Surface energies and preferred orientation

The observed preferred orientation of all of the films in this work, makes more sense in light of comparison of surface energies of the surfaces of ZB and W ZnS. In a paper by K. Wright et. al [60], the surface energies of sphalerite ZnS are simulated atomically, and the energies for different orientations are calulated, both in a pure stoichiometric environment, but also in Zn poor and Zn rich environments. Their results state that the 110 surfaces are the most stable in a stiochiometric environment, but the 111 and $\bar{1}\bar{1}\bar{1}$ surfaces are the most stable in a Zn poor and Zn rich environments, respectively. Since the EDS data from the target tells that it is sulfur-rich, this makes an argument for the observed orientation in the case that there is a ZB phase in the film. Another factor that could lead to an initially sulfur-rich environment, is a slight difference in ablation rate of Zn and S, or different sticking coefficient when either reach the substrate.

As mentioned by Zhang et. al. [61], calculations of average surface energies of zinc blende and wurtzite, are inconsistent with experimental work. Calculations say that the zinc blende structure is the lower energy one, but experiment says otherwise. The ZnS films grown in this work agrees with this for the experimental part, in that all films most probably are at least partially wurtzite.

5.10 Size dependence of ZnS phase stability

In the bulk, the transition temperature(T_c) from zinc blende to wurtzite is 1020 °C. However, in the films grown, a wurtzite phase is formed at substrate temperatures of 550 °C and lower. Work done by Li et. al. [62] can perhaps shed some light on this. Their results show that T_c is highly dependent on the particle size, be it nanocrystals or nanobelts. T_c shows a dramatic drop as the particle size decreases, and for nanoparticles 15 nm in diameter at 800 K, the preferred structure is wurtzite. Although these are different from thin films several hundred nanometers thick, the thin films may have nanocrystalline properties, especially in their initial growth phase as shown on silicon (100) (figure 4.6). However, this is merely a suggestion, and much further investigation would be needed to say anything more about this.

Chapter 6

Conclusion

6.1 Epitaxial ZnS film growth

The orientation of ZnS films grown under various conditions by PLD is not very sensitive to substrate preparation and orientation. Under various conditions, ZnS thin films have the same ZB(111)/W(002) preferred orientation. Films grown on silicon (100) grow by 3D-islands and have a dense nanocrystalline structure. Films grown on silicon (111) appear much smoother and ordered, although the grain structure. For this particular reason, silicon (111) substrates will be preferable for ZnS thin film growth, unless a way to grow films on silicon (100) with the same orientation and better quality is found.

6.2 In-situ native oxide removal

Even though the experiments were not a great success in terms of epitaxial film deposition, they demonstrate the principle that is is indeed possible to sputter the substrate surface in-situ in a PLD system, without adding extra components to it. By tuning the parameters in the sputtering phase and monitoring the surface closely by RHEED, it may be possible to obtain a clean and flat surface, whithout the use of hazardous chemicals, such as HF.

6.3 Substrate preparation

Even though the ZnS thin films are not shown to be affected by substrate preparation, there are indications that the "house clean" is not a satisfactory substrate preparation method in terms of oxide removal, and that further work is necessary. If it is not established before a thin film deposition that the substrate surface is clean, such as by monitoring with RHEED,

it cannot be stated that the surface actually is clean. Not knowing whether a substrate surface is clean or not introduces an unknown into the process of thin film deposition.

Chapter 7

Further Work

7.1 General remarks

Experimental materials science is, in general, tedious work. My experience is that it takes a lot more time than expected. The training and learning how to use different techniques, equipment and characterisation instruments, is also very time consuming. In addition, a considerable amount of time is spent doing troubleshooting, required maintenance or simply dealing with malfunctioning equipment.

7.2 Experimental issues

There are several aspects of the equipment used in this work, where there is room for improvement.

7.2.1 Pressure gauge on the load lock

The pressure gauge on the load lock of the PLD system has a lower limit of $5 \cdot 10^{-4}\mathrm{mbar}$, which means that when the pressure is below this value, one does not actually know the pressure inside the load lock (which is most of the time, since it only takes a few minutes to get below this value). To save time and actually know when the pressure in the load lock is low enough for heater transfer to the chamber, a pressure gauge with a different range should be used. These are commonplace parts in any vacuum system. Knowing the actual pressure in the load lock, and setting a maximum heater transfer pressure, may also give better control of the background pressure in the main chamber. This in turn may improve sample reproducibility, if done systematically.

7.2.2 Heater, heater stage and transfer arm

It can sometimes take hours (sic!) to transfer the sample from the load lock to the main chamber. Since the heater itself is taken out for every experiment, it has to be transferred across the chamber from the load lock and onto the heater stage inside the main chamber, using a transfer arm. The heater stage has coordinates x, y, and z, as well as a tilt angle. The main issue is the unpredictable behaviour of the stage; even with apparently the exact same coordinates and conditions used in an experiment the previous day, sometimes the heater will not load. By looking inside the chamber with the heater close to the heater stage, one simply does not understand how these settings worked only one day ago. Forcing the heater onto the stage may result in broken parts and/or bending of the thermocouple. The latter happened several times, resulting in an aborted experiment and having to vent the chamber to fix the thermocouple, wasting several days of work.

7.2.3 Heater and sample mounting

The temperature setting of the heater and the actual temperature of a mounted silicon substrate usually differ. The problem in this system, is that this difference is not systematic for identical samples. This may be due to differences in contact between the thermocouple and the heater, again due to the heater not loading in the same manner for every experiment. There will also be slight differences in the way the tantalum clamp holds the sample in place, because it is mounted manually with a screw. Where it sits on the substrate, how hard it pushes onto the substrate, and if the edge of the clamp is flat on the substrate or slightly tilted, can all affect the heat transfer between heater and substrate. Pyrometer measurements suggest that there can be temperature differences as high as $50\,^{\circ}\mathrm{C}$ on a $1\,\mathrm{cm}^2$. Therefore, a mounting system which provides good thermal contact from heater to substrate as well as little temperature variation on the substrate, would be an advantage.

7.2.4 RHEED equipment

Even though for the experiments in this work, the film growth on silicon (100) is clearly 3-dimensional, if one were to do experiments and achieve layer-by-layer growth with potentially observable RHEED oscillations and detection of growth modes, the scanning of the target during deposition creates so much noise in the RHEED signal that it completely overshadows any other effects on the RHEED intensities. Although this was already a known issue, I was not informed. because of this, growth modes could not be observed through RHEED oscillations.

Another issue is that the fluorescent screen in the PLD vacuum chamber has no shutter, and so it is constantly contaminated during any deposition, resulting in poor RHEED images, and eventually a useless screen. This can be seen in figure 4.14. A properly working shutter would be a nice addition to the system.

7.3 Film thickness uniformity

The thickness variations across relatively small samples, are significant. Although this has not been systematically investigated, it is evident from the performed experiments. There are several ways to improve film uniformity. One is to alter the plume itself, by changing the laser spot such that the plume is less directional. Another is to rotate and/or move the sample through different regions of the plume during deposition. A third possibility is to scan the laser beam itself, instead of moving the target, so that the center of the plume changes during deposition. None of these techniques were realisable in the PLD system used, because they require changing or adding entirely new components to the system. Achieving uniform deposition on small samples, as well as in situ thickness monitoring, would facilitate further analysis.

7.4 Future ZnS growth on silicon and characterization

Investigating the very initial phase of growth of ZnS films on silicon (100) could be interesting. Very thin films could be grown, and characterized by atomic force microscopy with gradually increasing thicknesses. This may shed some light on what is obstructing the influence of the (100) substrate. Transmission electron microscopy could perhaps be used to determine the phase and orientation of the very small grains in the initial growth stages and the evolution of the films with increasing thickness.

7.5 Substrate preparation

Developing a substrate preparation method which consistently shows by measurement that the substrate is clean, and a procedure to verify this before thin film deposition, would be an advantage. If it is possible to develop such a technique for in-situ cleaning, it could have several advantages over conventional cleaning involving HF acid, in that there is no contamination between cleaning and deposition, and simply the fact that it makes the use of hazardous chemicals unnecessary.

Bibliography

[1] K. Tanabe et al. "High-efficiency InAs/GaAs quantum dot solar cells by MOCVD". In: *Photovoltaic Specialists Conference (PVSC), 2012 38th IEEE* (2012), pp. 001929–001930.

[2] T. Tanaka et al. "Development of ZnTe intermediate band solar cells". In: *Photovoltaic Specialists Conference (PVSC), 2010 35th IEEE* (2010), pp. 2974–2977.

[3] J. Britt and C. Ferekides. "Thin film CdS/CdTe solar cell with 15.8% efficiency". In: *Applied Physics Letters* 62.22 (1993), pp. 2851–2852.

[4] Anthony M. Diamond et al. "Copper-alloyed ZnS as a p-type transparent conducting material". In: *PHYSICA STATUS SOLIDI A-APPLICATIONS AND MATERIALS SCIENCE* 209.11 (2012), 2101–2107.

[5] C. Tablero. "Effects of the impurityhost interactions on the nonradiative processes in ZnS:Cr". In: *Journal of Applied Physics* 108.9 (2010).

[6] J.-K. Chung et al. "The epitaxial growth and optical properties of thin films, deposited by pulsed laser deposition". In: *Physica Scripta Volume T* 2010.T139 (2010), 014018 (4 pp.) –.

[7] Young-Zo Yoo et al. "Heteroepitaxy of Hexagonal ZnS Thin Films Directly on Si (111)". In: *Japanses Journal of Applied Physics* 42 (2003), pp. 7029–7032.

[8] Hidenori Hiramatsu et al. "Heteroepitaxial growth of single-phase zinc blende ZnS films on transparent substrates by pulsed laser deposition under {H2S} atmosphere". In: *Solid State Communications* 124.1011 (2002), pp. 411 –415.

[9] K.T Hillie, C Curren, and H.C Swart. "ZnS thin films grown on Si(100) by XeCl pulsed laser ablation". In: *Applied Surface Science* 177.12 (2001), pp. 73 –77.

[10] Wei Zhang et al. "Phase controlled synthesis and optical properties of thin films by pulsed laser deposition". In: *Materials Research Bulletin* 48.10 (2013), pp. 3843 –3846.

[11] S Yano et al. “Absorption and photocurrent properties of thin ZnS films formed by pulsed-laser deposition on quartz”. In: *Thin Solid Films* 423.2 (2003), pp. 273 –276.

[12] W. P. Shen and H. S. Kwok. “Crystalline phases of II-VI compound semiconductors grown by pulsed laser deposition”. In: *Applied Physics Letters* 65.17 (1994), pp. 2162–2164.

[13] Robert Eason. *Pulsed Laser Deposition of Thin Films*. John Wiley and Sons, 2007.

[14] Milton Ohring. *The Materials Science of Thin Films*. Academic Press, INC., 1992.

[15] *Face centered cubic structure*. accessed 1.5.2014. URL: http://en.wikipedia.org/wiki/File:Lattice_face_centered_cubic.svg.

[16] *Hexagonal lattice*. accessed 12.5.2014. URL: http://en.wikipedia.org/wiki/File:Hexagonal_latticeFRONT.svg.

[17] Mario Birkholz. *Thin Film Analysis by X-Ray Scattering*. Wiley-VCH, 2006. ISBN: 978-3-527-31052-4.

[18] *Close packing of spheres*. accessed 1.5.2014. URL: http://en.wikipedia.org/wiki/File:Close_packing_box.svg.

[19] Safa O. Kasap and Peter Capper. *Handbook of electronic and photonic materials*. Springer, 2006, pp. 54,327.

[20] T. M. BIENIEWSKI and S. J. CZYZAK. “Refractive Indexes of Single Hexagonal ZnS and CdS Crystals”. In: *J. Opt. Soc. Am.* 53.4 (1963), pp. 496–497.

[21] *Silicon diamond structure*. accessed 1.5.2014. URL: http://en.wikipedia.org/wiki/File:Silicon-unit-cell-3D-balls.png.

[22] *Zinc blende structure*. accessed 1.5.2014. URL: http://en.wikipedia.org/wiki/File:Sphalerite-unit-cell-3D-balls.png.

[23] *Wurtzite structure*. accessed 1.5.2014. URL: http://en.wikipedia.org/wiki/File:Wurtzite-unit-cell-3D-balls.png.

[24] K.H. Wedepohl. “The composition of the continental crust”. English. In: *Geochimica et Cosmochimica Acta* 59.7 (1995/04/), pp. 1217 –32.

[25] Robert Hull. *Properties of Crystalline Silicon*. INSPEC, 1999, p. 91.

[26] *Tetrahedral bonding*. accessed 1.5.2014. URL: http://en.wikipedia.org/wiki/File:Tetrahedral-3D-balls.png.

[27] Yu.G Sidorov et al. “The heteroepitaxy of IIVI compounds on the non-isovalent substrates (ZnTe/Si)”. In: *Thin Solid Films* 367.12 (2000), pp. 203 –209.

[28] R. B. Roberts, G. K. White, and T. M. Sabine. “Thermal expansion of zinc sulfide: 300-1300 K”. In: *Australian Journal of Physics* 34 (1981), pp. 701–706.

[29] M. Lippmaa et al. “Growth mode mapping of SrTiO3 epitaxy”. In: *Applied Physics Letters* 76.17 (2000), pp. 2439–2441.

[30] Daniel Magnflt. “Nucleation and stress generation in thin films deposited with a pulsed energetic deposition flux”. PhD thesis. Linkping University, 2013.

[31] Rodica Ghita et al. “Study of SiO2/Si Interface by Surface Techniques”. In: *Crystalline Silicon - Properties and Uses, Prof. Sukumar Basu (Ed.)* (2011).

[32] Amir H. Al-Bayati et al. “Composition and structure of the native Si oxide by high depth resolution medium energy ion scatering”. In: *Surface Science* 241 (1991), pp. 91 –102.

[33] Amir H. Al-Bayati, Kevin G. Orrman-Rossiter, and D.G. Armour. “Study of residual damage in Si(001) due to low energy (110 eV) Ar+ and Cl+ bombardment using medium energy ion scattering”. In: *Surface Science* 249.13 (1991), pp. 293 –312.

[34] M. J. Kim and R. W. Carpenter. “Composition and structure of native oxide on silicon by high resolution analytical electron microscopy”. In: *Journal of Materials Research* 5 (02 Feb. 1990), pp. 347–351. ISSN: 2044-5326.

[35] J. Wong et al. “High resolution electron microscopic and spectroscopic characterization of semi insulating polycrystalline silicon and its interface with single crystal silicon”. In: *Applied Physics Letters* 48.1 (1986), pp. 65–67.

[36] Ondrej L. Krivanek and Jerzy H. Mazur. “The structure of ultrathin oxide on silicon”. In: *Applied Physics Letters* 37.4 (1980), pp. 392–394.

[37] L. C. Feldman et al. “Use of Thin Si Crystals in Backscattering-Channeling Studies of the Si-Si02 Interface”. In: *Phys. Rev. Lett.* 41 (20 1978), pp. 1396–1399.

[38] S. I. Raider, R. Flitsch, and M. J. Palmer. “Oxide Growth on Etched Silicon in Air at Room Temperature”. In: *Journal of The Electrochemical Society* 122.3 (1975), pp. 413–418.

[39] H. R. Philipp and E. A. Taft. “An optical characterization of native oxides and thin thermal oxides on silicon”. In: *Journal of Applied Physics* 53.7 (1982).

[40] W Henrion et al. “Spectroscopic investigations of hydrogen termination, oxide coverage, roughness, and surface state density of silicon during native oxidation in air”. In: *Applied Surface Science* 202.34 (2002), pp. 199 –205.

[41] H. Okumura et al. “Comparison of conventional surface cleaning methods for Si molecular beam epitaxy”. In: *Journal of the Electrochemical Society* 144.11 (1997), pp. 3765 –8.

[42] A. Inam et. al. “Low magnetic flux noise observed in laser-deposited in situ films of YB2Cu3Oy and implications for high- Tc SQUIDs”. In: *Nature* 341 (), pp. 723–726.

[43] *PVD Products*. accessed 7.5.2014. URL: http://www.pvdproducts.com.

[44] Y Suda et al. "Preparation of high quality nitrogen doped TiO2 thin film as a photocatalyst using a pulsed laser deposition method". In: *THIN SOLID FILMS* 453 (2004), 162–166.

[45] YR Ryu et al. "Optical and structural properties of ZnO films deposited on GaAs by pulsed laser deposition". In: *JOURNAL OF APPLIED PHYSICS* 88.1 (2000), 201–204.

[46] G.C. Tyrrell et al. "Kinetic energy and mass distributions of ablated species formed during pulsed laser deposition". In: vol. 25. 2-4. 1994, pp. 247 –52.

[47] James A. Greer. "History and current status of commercial pulsed laser deposition equipment". In: *JOURNAL OF PHYSICS D-APPLIED PHYSICS* 47 (2014).

[48] A.C. Barato, H. Hinrichsen, and D.E. Wolf. "Rate equations and scaling in pulsed laser deposition". In: *Physical Review E (Statistical, Nonlinear, and Soft Matter Physics)* 77.4 (2008/04/), 041607 (8 pp.) –.

[49] Byungha Shin et al. "Comparison of morphology evolution of Ge(001) homoepitaxial films grown by pulsed laser deposition and molecular-beam epitaxy". In: *Applied Physics Letters* 87.18 (2005).

[50] Ayahiko Ichimiya and Philip I. Cohen. *Reflection High Energy Electron Diffraction*. Cambridge Unviersity Press, 2010. ISBN: 9780511735097.

[51] Dayong Guo. *An introduction to MBE growth*. accessed 1-5-2014. URL: http://www.phas.ubc.ca/~berciu/TEACHING/PHYS503/PROJECTS/dayong.pdf.

[52] Harland G. Tompkins and Eugene A. Irene. *Handbook of Ellipsometry*. 2005. ISBN: 0-8155-1499-9.

[53] Jesper Jung et al. *Ellipsometry*. accessed 1.5.2014. URL: http://homes.nano.aau.dk/kp/Ellipsometry/main.pdf.

[54] International Organization for Standardization (ISO). "ISO 14644-1:1999 Cleanrooms and associated controlled environments – Part 1: Classification of air cleanliness". In: (2008).

[55] J. Brandenburg et al. "Pulsed laser deposition of metals: consequences of the energy distribution within the laser spot on film growth". In: *Applied Physics A* 79.4-6 (2004), pp. 1005–1007.

[56] I.P. McClean et al. "Low temperature epitaxial deposition of ZnS onto (100) Si by RF magnetron sputtering and molecular beam epitaxy". In: *Journal of Crystal Growth* 143.34 (1994), pp. 172 –175.

[57] Katsuyuki Utani and Sadao Adachi. “HF-treated (111), (110) and (100)Si Surfaces Studied by Spectroscopic Ellipsometry”. In: *Japanse Journal of Applied Physics* 32 (1993).

[58] S. Gonda et al. “Sub-nanometer scale measurements of silicon oxide thickness by spectroscopic ellipsometry”. In: *Japanese Journal of Applied Physics, Part 2 (Letters)* 37.11B (1998), pp. 1418 –20.

[59] Hiroshi Tomita, Tadashi Kikuchi, and Keiichi Furuya. “Hydrogen Desorption Behaviors of HF-Treated Silicon Wafer”. In: *Japanese Journal of Applied Physics* 30.5R (1991), p. 897.

[60] K. Wright et al. “Simulation of the structure and stability of sphalerite (ZnS) surfaces”. In: *American Mineralogist* 83 (1998), pp. 141–146.

[61] Hengzhong Zhang et al. “Molecular Dynamics Simulations, Thermodynamic Analysis, and Experimental Study of Phase Stability of Zinc Sulfide Nanoparticles”. In: *Journal of Physical Chemistry B* 107.47 (2003), pp. 13051 –13060.

[62] S. Li, J.S. Lian, and Q. Jiang. “Modeling size and surface effects on ZnS phase selection”. In: *Chemical Physics Letters* 455.46 (2008), pp. 202 –206.